Inorganic Chemistry **2020**, *59*, 17746-17757

https://doi.org/10.1021/acs.inorgchem.0c02973

In Pursuit of Panchromatic Absorption in Metal Coordination Complexes: Experimental Delineation of the HOMO Inversion Model Using Pseudo-Octahedral Complexes of Diarylamido Ligands

Jason D. Braun, Issiah B. Lozada and David E. Herbert*

Department of Chemistry and the Manitoba Institute of Materials, University of Manitoba, 144 Dysart Road, Winnipeg, MB, R3T 2N2, Canada

*david.herbert@umanitoba.ca

ABSTRACT

The ability of a compound to broadly absorb light across the incident solar spectrum is an important design target in the development of molecular photosensitizers. The 'HOMO inversion' model predicts that for $[(tpy)_2Fe]^{2+}$ (tpy = 2,2':6',2''-terpyridine) compounds, adjusting the character of the highest occupied molecular orbital (HOMO) from metal-centered to ligand-centered can drastically improve photophysical properties by broadening absorption in the visible and increasing molar extinction coefficients. In an effort to experimentally realize strong, panchromatic absorption, a tridentate *N*^*N'*^*N* diarylamido ligand bearing flanking benzannulated *N*-heterocyclic donors ($^{t\mathrm{Bu}}$**L**) was used to prepare deeply colored, pseudo-octahedral coordination complexes of a range of first-row transition and main-group metals $[(^{t\mathrm{Bu}}\mathbf{L})_2M^{0/+}$; M = Fe, Co, Ni, Zn, Ga]. While the Fe(II) congener exhibits the sought-after broad absorption, isostructural and isoelectronic complexes of other first-row transition and main-group metals show vastly different absorption and redox properties. Density functional theory (DFT) calculations point towards the relative energies of the metal *d* orbitals and ligand orbitals as the source of major changes in electronic structure, confirming aspects and limitations of the predictive 'HOMO inversion' model in experimentally realized systems with implications for the design of abundant transition-metal sensitizers with broad, panchromatic absorptive properties.

INTRODUCTION

The development of molecular photosensitizers that can efficiently harvest incident solar radiation is critical to the widespread application of sustainable energy capture and light-driven synthesis including in dye-sensitized solar cells (DSSCs),[1,2] photoredox catalysis[3] and the on-site production of solar fuels.[4] To facilitate the electron-transfer required for such applications, photosensitizers must exhibit sufficiently long-lived charge-transfer (CT) lifetimes[5] but would also ideally be engineered to strongly absorb as much of the solar spectrum as possible.[6] Late, second and third-row transition metal coordination complexes (MCCs) supported by highly conjugated ligands successfully fulfill the first of these criteria. Accordingly, while creative ligand design has led to development of mid- and early-metal first-row photosensitizer candidates with potentially useful properties,[7–9] many of the presently most widely used sensitizers are MCCs based on Ru(II) and Ir(III) centers supported by *N*-heterocyclic or related conjugated, chelating ligands.[10–12] A potential limitation of many of these dyes, including recently reported examples based on abundant metals such as Zr,[7] Fe,[13] and Co,[14] is the absence of low-energy visible and near-infrared (NIR) light absorption that precludes exploitation of a significant portion of available solar photons and can contribute to low incident photon-to-current efficiencies.[15]

A variety of approaches to extending the wavelength range over which MCCs can strongly absorb have therefore been pursued. Some of the more successful examples include cyclometalated complexes bearing strong field ligands,[16] the use of ligands comprised of large, extended π-systems,[17] push-pull complexes[18] and/or multi-metallic assemblies.[19,20] For example, bimetallic Rh complexes supported by bridging 1,8-naphthyridine and formamidinate ligands have broad light-absorption profiles and long-lived charge-transfer states capable of facilitating electron-transfer reactivity.[15,21,22] Exchanging naphthyridine for a bridging benzo[*c*]cinnoline ligand

furthermore leads to panchromatic absorbing molecules that can photochemically catalyze H_2 evolution using low-energy light.[23] Bimetallic complexes with no metal-metal interaction can also show intense, low energy absorptions when paired with appropriately conjugated binucleating ligands. *Bis*-iron(II) and *bis*-ruthenium(II) complexes of cyclam-derived macrocyclic ligands with a tetraiminoethylene core (Figure 1, **A**), for example, exhibit strong, low energy metal-to-ligand charge transfer (MLCT) absorptions for both Fe_2 (λ = 874 nm, ε = 24 600 M^{-1} cm^{-1})[24] and Ru_2 (λ = 910 nm, ε = 19 000 M^{-1} cm^{-1})[25] complexes. Upon oxidation, the mixed valent Ru(II)/Ru(III) analog displays an even larger absorptive cross-section at slightly higher energy (λ = 805 nm, ε = 68 000 M^{-1} cm^{-1}), though the band is quite narrow (FWHM = ~ 50 nm).

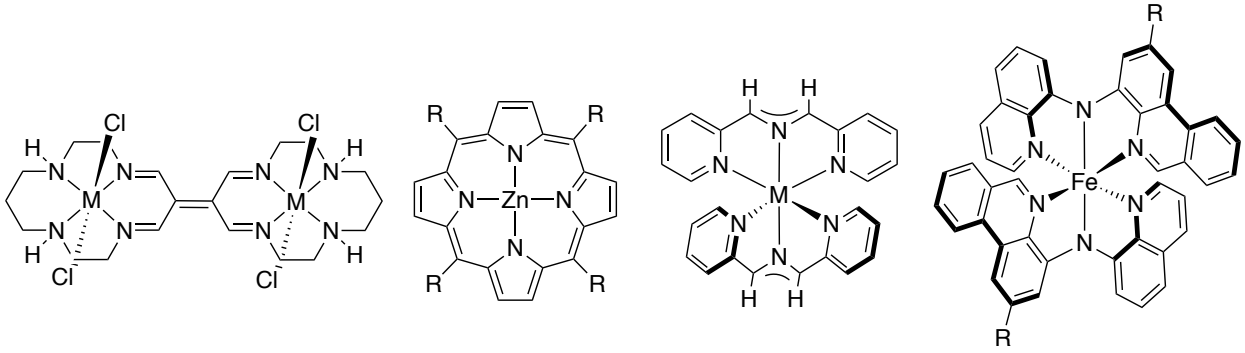

Figure 1. Selected design motifs for complexes that exhibit strong, low-energy absorption. Ranges of strong absorption (ε > 5 000 cm^{-1} M^{-1}): **A** (M = Fe: < 400 nm, 650 – 1000 nm,[24] M = Ru: < 450 nm, 750 – 1100 nm, upon single oxidation: < 450 nm, 720 – 900 nm[25]); **B** < 600 nm, depending on R group[26]; **C** (M = V: < 600 nm, M = Cr: < 825 nm, M = Mn: < 625 nm, M = Fe: < 650 nm, M = Co: < 650 nm, M = Ni: < 600 nm)[27]; **D** R = *t*Bu < 780 nm, R = CF_3 < 795 nm.[28]

MCCs supported by porphyrin ligands represent another strategy, owing to the intense absorption in the UV-visible region conferred by the conjugated macrocyclic ligand.[29] Solubility

of these highly planar complexes can present challenges,[30] though appending peripheral tethers to the porphyrin framework (Figure 1, **B**) can encourage solubility in common organic solvents with retention of favorable absorption properties.[26] As a result, substituted Zn-based porphyrins have been used as dyes in prototype DSSCs, enabling up to 7% power conversion efficiencies (η).[31] Absorption by metal-porphyrins, however, typically attenuates beyond 500-600 nm and this deficiency has been implicated in the relatively low η-values in comparison to DSSCs based on Ru-based MCC dyes.[26] Efforts to extend the absorption into the NIR by means of extended π-conjugation[32] or introduction of a push-pull system were found to be moderately successful, resulting in η-values of up to 13% for Zn porphyrins featuring a (2',4'-*bis*(hexyloxy)-[1,1'-biphenyl]-4-yl)amine donor.[33] Despite these advances, MCCs exhibiting strong and broad, panchromatic absorption remain quite rare, especially for mononuclear analogs based on abundant, first-row metals.

In seeking to outline a design strategy for iron-based sensitizers with improved optical properties, Jakubikova and coworkers highlighted the potential impact of altering the π-donor properties of 2,2':6',2"-terpyridine (tpy) ligands in pseudooctahedral $[bis(tpy)_2Fe]^{2+}$ complexes of Fe(II).[34] By computationally probing the energy match between occupied ligand orbitals of π-symmetry and the filled t_{2g}-type set on the d^6 metal, a model was developed in which better energy matching leads to stronger metal-ligand π-type interactions, increasing the energy of the highest occupied molecular orbital (HOMO) and fostering multiple mixed metal-to-ligand and intraligand charge transfer (MLCT/ILCT) transitions in the calculated spectrum. Further destabilization of ligand π-orbitals through π-extension at the tpy ligands was predicted to lead to full 'HOMO inversion' in which the HOMO becomes wholly ligand centered. An experimental example of this extreme that predated the computational study can be found in $(smif)_2Fe$[35] (Figure 1, **C**), where

'smif' is an azaallyl ligand *bis*[1,3-di(2-pyridyl)-2-azapropenide], first reported to be formed in the thermolysis of methylzinc *bis*(2-pyridylmemyl)amide.[36] For $(smif)_2Fe$, the HOMO and HOMO-1 are both ligand-centered, localized in the carbon-based nonbonding orbitals of the azaallyl moiety. As a result, very strong (ε = 40 000 – 60 000 M^{-1} cm^{-1}) interligand charge-tranfer (ILCT) transitions from these orbitals to π^* orbitals on the smif pyridine arms are observed,[27] reminiscent of those observed in complexes of dipyrromethane and related ligands.[37] These IL transitions extend the absorption spectra out to ~750 nm for $(smif)_2Fe$ and even further (~850 nm) for $(smif)_2Cr$ with strong absorptivity (ε = 6000 $M^{-1}cm^{-1}$) from 650 – 850 nm.[27]

We recently reported the construction of pseudo-octahedral iron complexes, $(^{R}\mathbf{L})_2Fe$ (R = *t*Bu, CF_3), where $^{R}\mathbf{L}$ is a benzannulated (4-phenanthridinyl)(8-quinolinyl)amido ligand (Figure 1, **D**).[28] These complexes exhibit nanosecond charge-transfer (CT) excited-state lifetimes and have broad absorptive cross-sections across the visible spectrum (ε > 5000 M^{-1} cm^{-1} from λ = 250 – 795 nm). The absorption properties are attributed to a combination of a π-extended ligand with strong acceptor properties and 'HOMO raising'. This can be thought of as an intermediate case of HOMO inversion, in which the energies of the HOMO through to HOMO-4 are spread out by strong mixing between Fe d and amido-based 2p orbitals.[38] Given recent exciting findings reported on sensitizer designs based on abundant transition elements beyond Group 8,[39,40] we set out to investigate how the identity of the metal center affects the redox chemistry and absorption profiles of complexes of $^{R}\mathbf{L}$ through changes to the dπ-pπ interaction induced by metal element selection and oxidation state. Here, we report the synthesis, characterization and electronic properties of a series of MCCs of the type $(^{t\mathrm{Bu}}\mathbf{L})_2M^{n+}$ (M = Fe, Co, Ni, Zn and Ga). In doing so, we attempt to experimentally delineate 'HOMO inversion'[34] design principles using a single ligand motif that

favors strong absorptivity,[41] and discuss the implications for the construction of panchromatic absorbing sensitizers using abundant metals beyond iron.

EXPERIMENTAL SECTION

Materials. Unless otherwise specified, all air sensitive manipulations were carried either in an N_2-filled glove box or using standard Schlenk techniques under Ar. $NiCl_2 \cdot 6H_2O$ (Alfa Aesar), $Co(acac)_3$ (acac = acetylacetonate), anhydrous $GaCl_3$ (Sigma Aldrich) and $Zn(NO_3)_2 \cdot 6H_2O$ (Fisher Scientific), were purchased and used without any further purification. Organic solvents were dried and distilled using appropriate drying agents prior to use. $^{t\mathrm{Bu}}\mathbf{L}$, $(^{t\mathrm{Bu}}\mathbf{L})_2\mathrm{Fe}$ and $[(^{t\mathrm{Bu}}\mathbf{L})_2\mathrm{Fe}][PF_6]$ were synthesized according to literature procedures.[28]

Instrumentation and Methods. For electrochemical analysis, 5-10 mg of each compound investigated was dissolved in 15 mL of 0.1 M $[n\mathrm{Bu}_4\mathrm{N}][PF_6]$ in CH_3CN and purged with Ar for 20 minutes before analysis. All electrochemical experiments were conducted under inert (Ar) atmosphere using a CHI 760c bipotentiostat, a 3 mm diameter glassy carbon working electrode, a Ag/Ag^+ quasi-non-aqueous reference electrode separated by a Vycor tip, and a Pt wire counter electrode. Cyclic voltammetric (CV) experiments were conducted using scan rates of 50-800 mV/s. Differential Pulse Voltammetry (DPV) experiments were also conducted, using a 5 mV increment, 50 mV amplitude, 0.1 s pulse width, 0.0167 s sample width, and 0.5 s pulse period. Upon completion of all CV and DPV analyses, ferrocene (FcH) was added to the solution as an internal standard, with all potentials reported versus the $FcH^{0/+}$ redox couple. 1- and 2D NMR spectra were recorded on Bruker Avance 300 MHz or Bruker Avance – III 500 MHz spectrometers. ^1H and $^{13}C\{^1H\}$ NMR spectra were referenced to residual solvent peaks. Elemental analysis was

performed at the University of Manitoba using a Perkin Elmer 2400 Series II CHNS/O Elemental Analyzer. Electronic absorption spectra were recorded on an Agilent Technologies Cary 5000 Series UV-Vis-NIR spectrophotometer in dual beam mode (range: 230–1600 nm). Spectroelectrochemical experiments were performed using a Jasco-V770 spectrophotometer using a CHI-620 C electrochemical analyzer and a custom-made cell. A three-electrode system of platinum working, auxiliary and Ag/Ag^+ reference electrodes was used.

Synthesis of $[(^{tBu}\mathbf{L})_2Co][PF_6]$: A 250 mL round-bottom flask was charged with $Co(acac)_3$ (0.069 g, 0.19 mmol), $^{tBu}\mathbf{L}$ (0.15 g, 0.40 mmol), and $Na[PF_6]$ (0.033 g, 0.19 mmol). MeOH (50 mL) was added and the flask was stirred and refluxed at 100 °C overnight. The flask was then cooled to room temperature and stirred for 1 h. The solution was then concentrated and added dropwise to a stirring solution of pentane (100 mL). The red precipitate was then filtered and washed with Et_2O (3 x 20 mL). Isolated yield = 0.167 g (90 %).

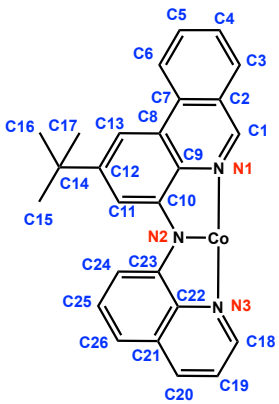

^1H NMR ($CDCl_3$, 500 MHz): δ 8.66 (d, 2H, J_{HH} = 1.5 Hz, C_{13}-H), 8.50 (d, 2H, J_{HH} = 8.3 Hz, C_3-H), 8.48 (d, 2H, J_{HH} = 8.1 Hz, C_{26}-H), 8.35 (s, 2H, C_1-H), 8.10-8.03 (m, 4H, C_{18}-H, C_{20}-H), 7.93 (s, 2H, C_{11}-H), 7.89 (t, 2H, J_{HH} = 8.1 Hz, C_{25}-H), 7.80 (ddd, 2H, J_{HH} = 8.3, 6.9, 1.3 Hz, C_4-H), 7.63 (dd, 2H, J_{HH} = 8.2, 1.3 Hz, C_6-H), 7.53 (ddd, 2H, J_{HH} = 8.0, 6.8, 0.9 Hz, C_5-H), 7.25 (d, 2H, J_{HH} = 7.8 Hz, C_{24}-H), 7.16 (dd, 2H, J_{HH} = 8.2, 5.3 Hz, C_{19}-H), 1.74 ppm (s, 18H, $C_{15, 16, 17}$-H). $^{13}C\{^1H\}$ NMR ($CDCl_3$, 125 MHz): δ 154.9 (C_{12}), 151.8 (C_1), 148.3 (C_{20}), 148.0 (C_{10}), 147.7 (C_{23}), 147.5 (C_{22}), 139.5 (C_9), 139.2 (C_{18}), 133.5 (C_4), 132.9 (C_7), 131.4 (C_{21}), 130.8 (C_{25}), 129.5 (C_6), 128.4 (C_5), 127.0 (C_3), 126.9 (C_8), 123.4 (C_{19}), 122.5 (C_3), 116.3 (C_{24}), 114.9 (C_{26}), 113.2 (C_{13}), 108.6

(C_{11}), 36.2 (C_{14}), 32.0 ppm ($C_{15,16,17}$). UV-vis (CH_3CN): λ (ε) 308 (41 880), 390 (9 670), 510 nm (23 310 M^{-1} cm^{-1}). Anal. Calcd for $CoC_{52}H_{44}N_6PF_6$: C, 65.27; H, 4.64. Found: C, 65.13; H, 4.64.

Synthesis of (^{tBu}**L**)$_2$Ni: A 250 mL round-bottom flask was charged with $NiCl_2 \cdot 6H_2O$ (0.06 g, 0.25 mmol), ^{tBu}**L** (0.200 g, 0.53 mmol), and NaO*t*Bu (0.051 g, 0.53 mmol). MeOH (50 mL) was added and the flask was stirred and refluxed at 100 °C overnight. The flask was then cooled to room temperature and stirred for 1 h. The solvent was then removed and the red compound was dissolved again in minimal CH_2Cl_2 (5 mL) and precipitated by the addition of cold pentane (50 mL). The resulting suspension was filtered and the solid compound then extracted off of the filter using CH_2Cl_2. This solution was then dried to give a bright red solid. Isolated yield = 0.160 g (78 %). ^{1}H NMR ($CDCl_3$, 300 MHz): δ 43.0 (br), 32.4 (br), 29.3 (br), 19.8 (br), 17.3 (br), 12.9 (s), 12.0 (br), 10.3 (s), 5.7 (br), 2.0 ppm (s). UV-vis (CH_3CN): λ (ε) 289 (51 330), 318 (32 190), 405 (10 280), 519 nm (28 370 M^{-1} cm^{-1}). μ_{eff} (Evans method) = 2.90 μ_B. Anal. Calcd for $NiC_{52}H_{44}N_6$: C, 76.95; H, 5.46. Found: C, 77.07; H, 5.47.

Synthesis of (^{tBu}**L**)$_2$Zn: A 250 mL round-bottom flask was charged with $Zn(NO_3)_2 \cdot 6H_2O$ (0.077 g, 0.26 mmol), ^{tBu}**L** (0.200 g, 0.53 mmol), and NaO*t*Bu (0.051 g, 0.53 mmol). MeOH (50 mL) was added and the flask was stirred and refluxed at 100 °C overnight. The flask was then cooled to room temperature and stirred for 1 h where a red precipitate formed. The mixture was then filtered over celite and extracted with dichloromethane. The filtrate was concentrated and put in the freezer overnight. The resulting precipitate was subject to the same treatment. Isolated yield = 0.191 g (91 %). ^{1}H NMR ($CDCl_3$, 300 MHz): δ 8.57 (s, 2H,

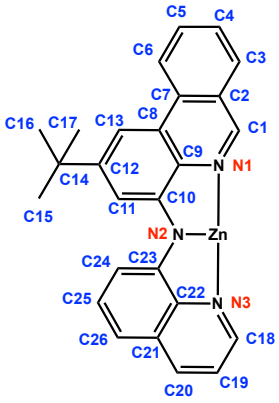

C_{13}-H), 8.52 (d, 2H, J_{HH} = 8.4 Hz, C_3-H), 8.46 (s. 2H, C_1-H), 8.26 (d, 2H, J_{HH} = 7.9 Hz, C_{26}-H), 8.06 (dd, 2H, J_{HH} = 4.4, 1.7 Hz, C_{18}-H), 7.90 (dd, 2H, J_{HH} = 8.2, 1.7 Hz, C_{20}-H), 7.77 (d, 2H. J_{HH} = 1.8 Hz, C_{11}-H), 7.69-7.61 (m, 4H, C_4-H, C_{25}-H), 7.58-7.54 (m, 2H, C_6-H), 7.40 (t, 2H, J_{HH} = 7.6 Hz, C_5-H), 6.94 (dd, 4H, J_{HH} = 8.1, 4.1 Hz, C_{19}-H, C_{24}-H) 1.66 ppm (s, 18H, $C_{15, 16, 17}$-H). ^{13}C {^1H} NMR ($CDCl_3$, 125 MHz): δ 151.8 (C_{12}), 147.3 (C_{10}), 147.3 (C_{23}), 146.7 (C_1), 144.2 (C_{18}), 141.2 (C_{22}), 137.0 (C_{20}), 134.3 (C_9), 133.8 (C_7), 130.8 (C_4), 130.3 (C_{21}), 129.2 (C_{25}), 129.1 (C_6), 126.6 (C_5), 126.5 (C_2), 125.0 (C_8), 122.3 (C_3), 121.2 (C_{19}), 111.2 (C_{24}), 109.5 (C_{13}), 108.7 (C_{26}), 103.6 (C_{11}), 36.0 (C_{14}), 32.0 ppm ($C_{15, 16, 17}$). Note: numbering scheme shown for UV-vis (CH_3CN): λ (ε) 314 (33 000), 393 (19 880), 503 nm (24 040 M^{-1} cm^{-1}). Anal. Calcd for $ZnC_{52}H_{44}N_6$: C, 76.32; H, 5.42. Found: C, 76.18; H, 5.39.

Synthesis of [(**^{tBu}L**)$_2$Ga][PF_6]: A 100 mL Teflon stoppered flask was charged with $GaCl_3$ (0.023 g, 0.13 mmol), **^{tBu}L** (0.1 g, 0.26 mmol), NaO*t*Bu (0.025 g, 0.26 mmol), Na[PF_6] (0.22 g, 0.13 mmol), and THF (20 mL). The flask was placed in an oil bath at 100 °C and stirred overnight. The solvent was the removed and the orange solid dissolved in CH_2Cl_2 (20 mL), filtered over a pad of celite, and pumped dry leaving a bright orange solid. Isolated yield = 0.112 g (88 %). ^1H NMR (CD_2Cl_2, 500 MHz): δ 8.72 (d, 2H, J_{HH} = 1.7 Hz, C_{13}-H), 8.66 (d, 2H, J_{HH} = 8.4 Hz, C_3-H), 8.58 (s, 2H, C_1-H), 8.52 (d, 2H, J_{HH} = 8.0 Hz, C_{26}-H), 8.32 (dd, 2H, J_{HH} = 8.3, 1.6 Hz, C_{20}-H), 8.20 (dd, 2H, J_{HH} = 4.8, 1.6 Hz, C_{18}-H), 8.11 (d, 2H, J_{HH} = 1.7 Hz, C_{11}-H), 7.98 – 7.83 (m, 4H, C_4-H, C_{25}-H), 7.76 (d, 2H, J_{HH} = 8.0 Hz, C_6-H), 7.61 (t, 2H, J_{HH} = 7.5 Hz, C_5-H), 7.40 (d, 2H, J_{HH} = 8.3 Hz, C_{24}-H), 7.27 (dd, 2H, J_{HH} = 8.2, 4.8 Hz, C_{19}-H) 1.74 ppm (s, 18H, $C_{15, 16, 17}$). ^{13}C {^1H} NMR (CD_2Cl_2, 125 MHz): δ 154.6 (C_{12}), 146.9 (C_1), 143.6 (C_{18}), 141.9

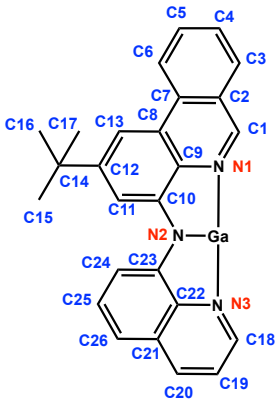

(C_{23}), 141.6 (C_{10}), 141.3 (C_{20}), 137.1 (C_{21}), 134.6 (C_9), 133.9 (C_4), 130.9 (C_{25}), 130.6 (C_{22}), 130.4 (C_6), 129.9 (C_7), 128.7 (C_5), 126.3 (C_2), 126.2 (C_8), 122.9 (C_3), 122.6 (C_{19}), 116.0 (C_{24}), 111.8 (C_{26}), 110.9 (C_{13}), 108.1 (C_{11}), 36.6 (C_{14}), 31.9 ppm ($C_{15, 16, 17}$). UV-vis (CH_3CN): λ (ε) 280 (42 710), 324 (20 510), 359 (8 610), 372 (9 050), 472 nm (17 220 M^{-1} cm^{-1}). Anal. Calcd for $GaC_{52}H_{44}N_6PF_6$ (CH_2Cl_2 x 1): C, 60.48; H, 4.40. Found: C, 60.29; H, 4.29.

X-Ray Crystallography

X-ray data was collected from multi-faceted crystals of suitable size and quality selected from a representative sample of crystals of the same habit using an optical microscope. Each crystal was mounted on a MiTiGen loop and data collection carried out in a cold stream of nitrogen (150 K; Bruker D8 QUEST ECO; Mo K_α radiation). All diffractometer manipulations were carried out using Bruker APEX3 software.[42] Structure solution and refinement was carried out using XS, XT and XL software, embedded within OLEX2.[43] For each structure, the absence of additional symmetry was confirmed using ADDSYM incorporated in the PLATON program.[44] CCDC Numbers 2022989-2022991 contain the supplementary crystallographic data for this paper. These data can be obtained free of charge from The Cambridge Crystallographic Data Center via www.ccdc.cam.ac.uk/structures.

Crystal structure data for [($^{t\mathrm{Bu}}$**L**)$_2$Co][PF_6] (CCDC 2022989): Crystals were grown by slow diffusion of pentane into a saturated solution of fluorobenzene. Red blocks; $C_{52}H_{44}N_6F_6PCo$ 956.83 g mol^{-1}, monoclinic, space group *C*2/*c*; *a* = 24.9037(13) Å, *b* = 11.5317(7) Å, *c* = 19.7403(11) Å, $\alpha = \gamma = 90°$, β = 93.041(3), V = 5661.1(6) $Å^3$; Z = 4, ρ_{calcd} = 1.123 g cm^{-3}; crystal dimensions 0.200 x 0.100 x 0.070 mm; $2\theta_{max}$ = 58.158°; 39165 reflections, 6523 independent (R_{int}

= 0.0782), intrinsic phasing; absorption coeff (μ = 0.387 mm^{-1}), absorption correction semi-empirical from equivalents (SADABS); refinement (against F_o^2) with SHELXTL V6.1, 328 parameters, 0 restraints, R_1 = 0.0673 ($I > 2\sigma$) and wR_2 = 0.1705 (all data), Goof = 1.143, residual electron density 0.36/−0.45$Å^{-3}$. Residual solvent molecules were not able to be modelled successfully. Two solvent voids of 839 $Å^3$ each containing an electron density of 180 e^- was dealt with using the SQUEEZE protocol included in the PLATON program.

Crystal structure data for [($^{t\mathrm{Bu}}$**L**)$_2$Ni] (CCDC 2022990): Crystals were grown by slow evaporation of a saturated pentane solution. Red blocks; $C_{52}H_{44}N_6Ni$ 811.64 g mol^{-1}, triclinic, space group *P*-1; *a* = 11.7853(4) Å, *b* = 11.9157(4) Å, *c* = 16.3161(5) Å, *α* = 85.686(2)º, β = 85.655(2)º, *γ* = 74.584(2)°, V = 2198.87(13) $Å^3$; Z = 2, ρ_{calcd} = 1.226 g cm^{-3}; crystal dimensions 0.300 x 0.250 x 0.150 mm; $2\theta_{max}$ = 66.538°; 141096 reflections, 16881 independent (R_{int} = 0.0503), intrinsic phasing; absorption coeff (μ = 0.483 mm^{-1}), absorption correction semi-empirical from equivalents (SADABS); refinement (against F_o^2) with SHELXTL V6.1, 538 parameters, 0 restraints, R_1 = 0.0509 ($I > 2\sigma$) and wR_2 = 0.1305 (all data), Goof = 1.028, residual electron density 1.05 /−0.57$Å^{-3}$. Residual solvent molecules were not able to be modelled successfully. A solvent void of 252 $Å^3$ containing an electron density of 49 e^- was dealt with using the SQUEEZE protocol included in the PLATON program.

Crystal structure data for [($^{t\mathrm{Bu}}$**L**)$_2$Ga][PF_6] (CCDC 2022991): Crystals were grown by slow evaporation of diethyl ether into a saturated dichloromethane solution. Orange blocks; $C_{52}H_{44}N_6F_6PGa$ 967.63 g mol^{-1}, monoclinic, space group *C*2/*c*; *a* = 18.29(2) Å, *b* = 16.66(2) Å, *c* = 16.81(2) Å, *α* = *γ* = 90°, β = 99.338(18)º, V = 5055(12) $Å^3$; Z = 4, ρ_{calcd} = 1.226 g cm^{-3}; crystal

dimensions 0.170 x 0.080 x 0.030 mm; $2\theta_{max}$ = 55.29°; 63854 reflections, 5863 independent (R_{int} = 0.1402), intrinsic phasing; absorption coeff (μ = 0.855 mm^{-1}), absorption correction semi-empirical from equivalents (SADABS); refinement (against F_o^2) with SHELXTL V6.1, 330 parameters, 0 restraints, R_1 = 0.0533 ($I > 2\sigma$) and wR_2 = 0.1242 (all data), Goof = 1.059, residual electron density 0.75 /−0.65 $Å^{-3}$.

RESULTS AND DISCUSSION

In selecting metal ions for our series, we focused on first-row transition metals with *d*-electron counts that favor metal-to-ligand type charge transfer transitions that typically form the basis of sensitization using MCCs [*i.e.*, d^6: Fe(II), Co(III); d^8: Ni(II)].[45] To round out these selections, two d^{10} metal ions were included, Zn(II) and Ga(III), to probe how a templating ion might facilitate solely intra- or inter-ligand transitions in the absence of energetically accessible *d*-electrons. The synthesis of the benzannulated, phenanthridine-based diarylamido pincer-type ligand ($^{t\mathrm{Bu}}$**L**) and its neutral Fe(II) and cationic complexes [($^{t\mathrm{Bu}}$**L**)$_2$Fe] and [($^{t\mathrm{Bu}}$**L**)$_2$Fe][PF_6] has been described.[28] Pseudo-octahedral complexes of $^{t\mathrm{Bu}}$**L** with Ni(II), Zn(II) and Co(III) were prepared by the addition of two equivalents of the proligand $^{t\mathrm{Bu}}$**LH** to the appropriate metal salt in refluxing methanol (Scheme 1). The Ga(III) salt was similarly prepared using dry THF at reflux. Where necessary, an exogenous Brønsted base was also present.

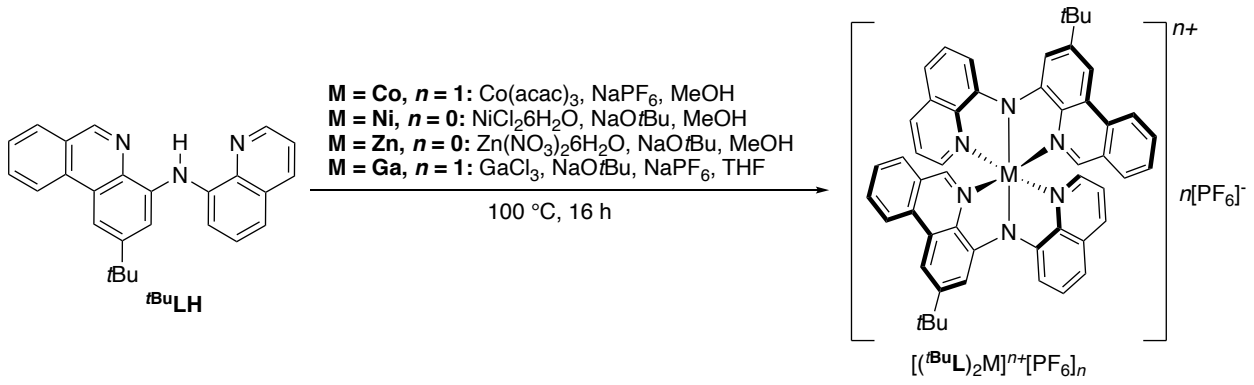

Scheme 1. Synthesis of homoleptic metal coordination complexes described in this work. For M = Fe (n = 0, 1) see reference[28].

In all cases, the formation of the desired compounds was followed by the appearance of a strongly colored solution and the loss of the amine N-*H* proligand peak in the ^{1}H NMR spectra. Paramagnetism was observed for ($^{t\mathrm{Bu}}$**L**)$_2$Ni and reaction progress was therefore determined by loss of peaks attributed to free proligand in the diamagnetic range of the ^{1}H NMR spectrum. ^{1}H and ^{13}C NMR spectra of each diamagnetic complex showed a single ligand environment, suggesting magnetic equivalence in solution on the NMR timescale. A downfield ^{1}H shift of the proton nucleus in the 6-position of the phenanthridinyl arm (*ortho* to the N donor atom) was found to be diagnostic of compound identity (δ / ppm = 8.54 ($^{t\mathrm{Bu}}$**L**)$_2$Fe; 8.66 [($^{t\mathrm{Bu}}$**L**)$_2$Co][PF$_6$]; 8.57 ($^{t\mathrm{Bu}}$**L**)$_2$Zn; 8.72 [($^{t\mathrm{Bu}}$**L**)$_2$Ga][PF$_6$]). The neutral Fe complex is susceptible to oxidation in ambient aerobic conditions, while each of the remaining complexes were found to be stable in the presence of both air and moisture in solution and the solid-state. Combustion analysis of the isolated products confirmed the purity of each bulk sample in the solid state.

Solid-State Structures of [($^{t\mathrm{Bu}}$**L**)$_2$**M**]$^{n+}$[**PF$_6$**]$_n$

The solid-state structures of three of the MCCs ([($^{t\mathrm{Bu}}$**L**)$_2$Co][PF$_6$], ($^{t\mathrm{Bu}}$**L**)$_2$Ni and [($^{t\mathrm{Bu}}$**L**)$_2$Ga][PF$_6$]) were determined using single crystal X-ray diffraction (Figure 2). In each

structure, the metal is arranged in a pseudo-octahedral coordination environment, with amido nitrogen (N_{amido}) atoms located *trans* to one another. Bond distances and angles are summarized in Table S1. A significantly larger coordination sphere is observed for the Ni and Ga complexes in comparison to earlier transition metal analogs, as seen through the length of all M-N bonds. The gallium and nickel complexes exhibit similar bond distances between the metal and neutral nitrogen donors (~2.07 Å), but the anionic Ga-N_{amido} [1.958(3) Å] separations are smaller compared to Ni-N_{amido} [2.0168(13), 2.0161(13) Å]. This is consistent with the increased positive charge at the higher oxidation state Ga(III). In general, the M-N_{amido} distance is the shortest M-N contact within each molecule and is significantly shorter yet for the Group 8/9 transition metal analogs following the trend Fe[28] ≈ Co < Ga < Ni. The two d^6 congeners, ($^{t\mathrm{Bu}}$**L**)$_2$Fe[28] and [($^{t\mathrm{Bu}}$**L**)$_2$Co][PF_6], show only minor differences in bond lengths to the central metal, with a tighter coordination environment seen with Co, befitting the larger positive charge on Co(III). The coordination sphere observed for these molecules correlate strongly with trends in metal ionic radii[46] with the rigid nature of the ligand enforcing smaller ligand bite angles in the complexes of larger metal ions[47] (Ga/Ni ~160º, Fe ~166°,[28] Co ~170°).

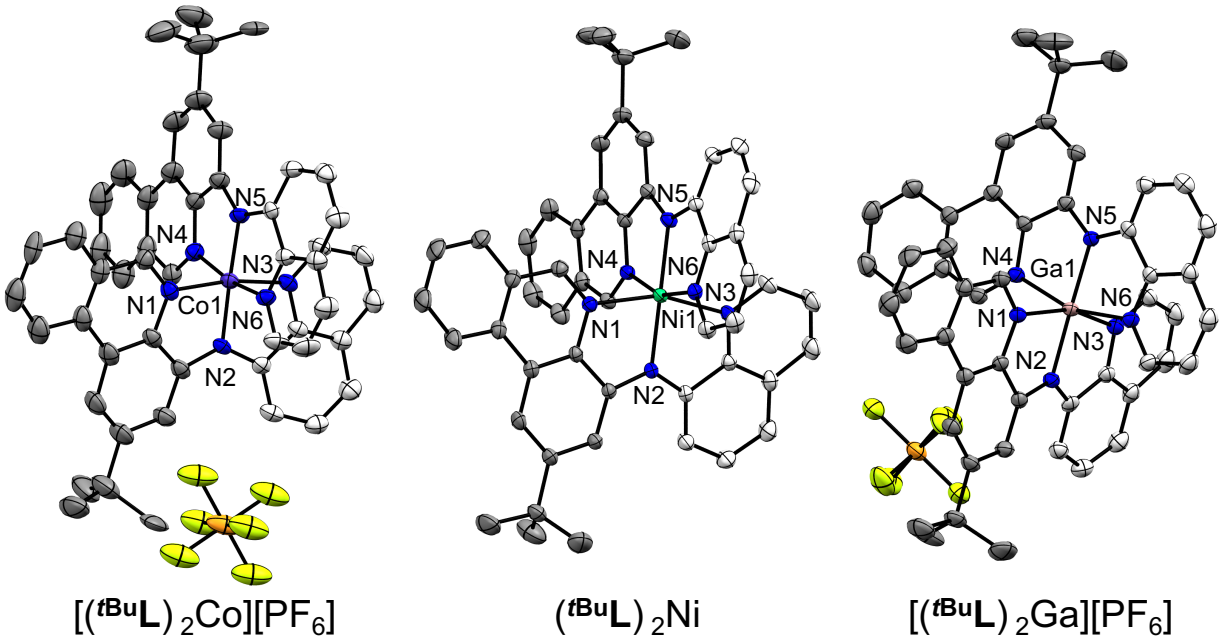

Figure 2. Crystal structures of $[(^{t\mathrm{Bu}}\mathbf{L})_2\mathrm{M}]^{n+}[\mathrm{PF_6}]_n$ (M = Co, n = 1; M = Ni, n = 0; M = Ga, n = 1) with thermal ellipsoids shown at 50% probability levels. Hydrogen atoms, select atom labels and co-crystallized solvent molecules are omitted for clarity. Selected bond distances (Å) and angles (°): $[(^{t\mathrm{Bu}}\mathbf{L})_2\mathrm{Co}][\mathrm{PF_6}]$ Co1-N1 1.908(3), Co1-N4 1.908(3), Co1-N2 1.897(2), Co1-N5 1.897(2), Co1-N3 1.915(3), Co1-N6 1.915 (3), N1-Co1-N3 169.50(11), N4-Co1-N6 169.50(11), N2-Co1-N5 178.10(17); $(^{t\mathrm{Bu}}\mathbf{L})_2\mathrm{Ni}$ Ni1-N1 2.0707(13), Ni1-N4 2.0783(13), Ni1-N2 2.0167(12), Ni1-N5 2.0160(13), Ni1-N3 2.0761(13), Ni1-N6 2.0720(13), N1-Ni1-N3 159.76(5), N4-Ni-N6 160.25(5), N2-Ni1-N5 178.23(5); $[(^{t\mathrm{Bu}}\mathbf{L})_2\mathrm{Ga}][\mathrm{PF_6}]$ Ga1-N1 2.074(3), Ga1-N4 2.074(3), Ga1-N2 1.958(3), Ga1-N5 1.958(3), Ga1-N3 2.074(3), Ga1-N6 2.074(3), N1-Ga1-N3 161.66(10), N4-Ga1-N6 161.66(10), N2-Ga1-N5 178.89(15).

Electronic Structures

While the solid-state structures of $[(^{t\mathrm{Bu}}\mathbf{L})_2\mathrm{M}]^{n+}[\mathrm{PF_6}]_n$ do not vary significantly, the complexes show interesting differences in their colors and therefore in their electronic absorption spectra. All are deeply colored thanks to the benzannulated ligand framework of $^{t\mathrm{Bu}}\mathbf{L}$, but the metal identity strongly influences each absorption profile. When the central metal is Co(III), Ni(II) or Zn(II), the resultant $[(^{t\mathrm{Bu}}\mathbf{L})_2\mathrm{M}]^{n+}[\mathrm{PF_6}]_n$ complexes are dark red both as amorphous powders and crystalline solids. In acetonitrile solution, the compounds all show high molar absorptivities (ε ~20 000-30 000 $\mathrm{M^{-1}\,cm^{-1}}$) for transitions in the visible range (~480-540 nm, Figure 3 and Table 1). The lowest energy absorptions for $[(^{t\mathrm{Bu}}\mathbf{L})_2\mathrm{Co}][\mathrm{PF_6}]$, $(^{t\mathrm{Bu}}\mathbf{L})_2\mathrm{Ni}$ and $(^{t\mathrm{Bu}}\mathbf{L})_2\mathrm{Zn}$ are all relatively narrow bands (FWHM = ~3290 $\mathrm{cm^{-1}}$), with maxima at ~500 nm. The λ_{max} for $[(^{t\mathrm{Bu}}\mathbf{L})_2\mathrm{Ga}][\mathrm{PF_6}]$ is blue-shifted (λ_{max} = 472 nm, ε = 17 220 $\mathrm{M^{-1}\,cm^{-1}}$) and the complex is accordingly a lighter orange to the eye. The proligand $^{t\mathrm{Bu}}\mathbf{LH}$ is a yellow solid, with a narrow λ_{max} of 388 nm (ε value of ~ 12 270 $\mathrm{M^{-1}\,cm^{-1}}$). In contrast, $(^{t\mathrm{Bu}}\mathbf{L})_2\mathrm{Fe}$ is deep green, showing true panchromatic absorption with a broad and large absorptive cross-section spanning across the visible.[28] Extending absorption of the solar spectra to 900 nm represents a doubling in both the number of harvestable photons and the theoretical incident photon-to-current efficiency when compared to dyes with absorption that attenuates at ~650 nm,[15] underscoring the motivation to design such complexes.

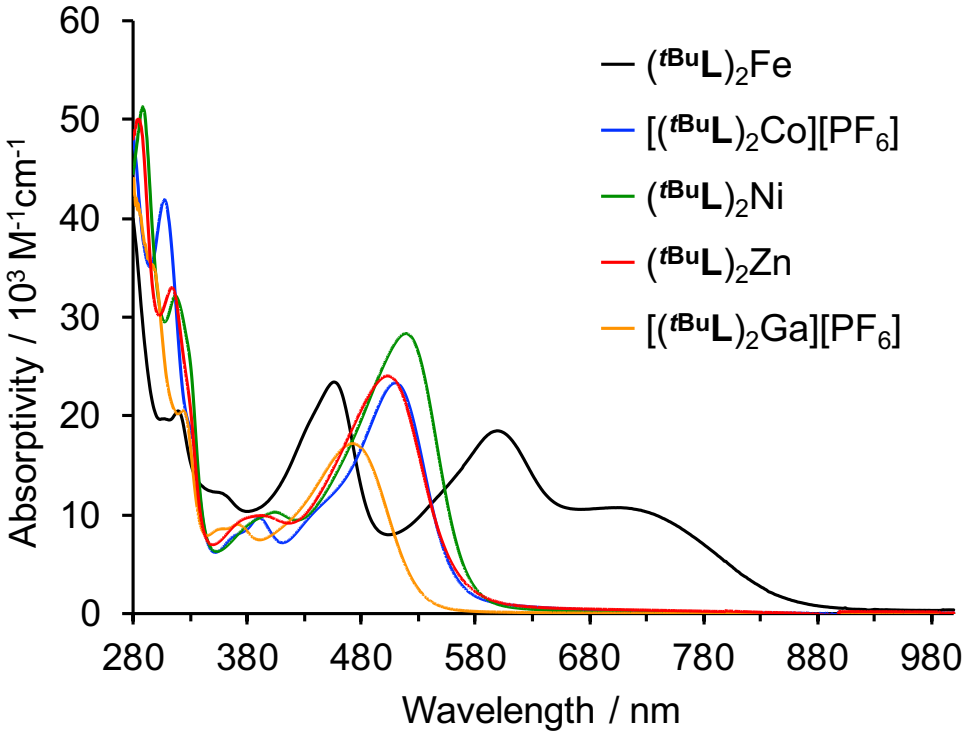

Figure 3. UV-Vis/NIR absorption spectra of $[(^{t\mathrm{Bu}}\mathbf{L})_2\mathrm{M}]^{n+}[\mathrm{PF_6}]_n$ in $\mathrm{CH_3CN}$ at 295 K.

Table 1. Redox potentials and electronic absorption spectral data for $[(^{t\mathrm{Bu}}\mathbf{L})_2\mathrm{M}]^{0/+}$

Compound	$E_{1/2}$/V[a]	λ/nm (ε/M^{-1}cm^{-1})[b]
$(^{t\mathrm{Bu}}\mathbf{L})_2\mathrm{Fe}$ /$[(^{t\mathrm{Bu}}\mathbf{L})_2\mathrm{Fe}][\mathrm{PF_6}]$	-2.59, -2.43, -0.77, 0.05, 0.70	$(^{t\mathrm{Bu}}\mathbf{L})_2\mathrm{Fe}$: 319 (26 310), 454 (26 030), 596 (17 990), 724 (8 510) $[(^{t\mathrm{Bu}}\mathbf{L})_2\mathrm{Fe}][\mathrm{PF_6}]$: 311 (34 950), 414, (22 810), 512 (12 430), 1024 (4 560)
$[(^{t\mathrm{Bu}}\mathbf{L})_2\mathrm{Co}][\mathrm{PF_6}]$	-2.23, -1.30 0.31, 0.50	$[(^{t\mathrm{Bu}}\mathbf{L})_2\mathrm{Co}][\mathrm{PF_6}]$: 308 (41 880), 390 (9 670), 510 (23 310)
$(^{t\mathrm{Bu}}\mathbf{L})_2\mathrm{Ni}$	-2.55, -2.42, -0.23, -0.04, 0.48	$[(^{t\mathrm{Bu}}\mathbf{L})_2\mathrm{Ni}]$: 289 (51 330), 318 (32 190), 405 (10 280), 519 (28 370)
$(^{t\mathrm{Bu}}\mathbf{L})_2\mathrm{Zn}$	-2.49, -2.38, -0.20, -0.07, 0.47	$[(^{t\mathrm{Bu}}\mathbf{L})_2\mathrm{Zn}]$: 314 (33 000), 393 (19 880), 503 (24 040)
$[(^{t\mathrm{Bu}}\mathbf{L})_2\mathrm{Ga}][\mathrm{PF_6}]$	-2.45, -2.13, -1.85, 0.42, 0.59	$[(^{t\mathrm{Bu}}\mathbf{L})_2\mathrm{Ga}][\mathrm{PF_6}]$: 280 (42 710), 324 (20 510), 472 (17 220)

[a] in $\mathrm{CH_3CN}$ with 0.10 M $[n\mathrm{Bu_4N}][\mathrm{PF_6}]$ as the supporting electrolyte using a glassy carbon working electrode and scan rates of 100 mV s^{-1}. Potentials are listed vs. $\mathrm{FcH}^{0/+}$.

[b] in $\mathrm{CH_3CN}$ at 295 K.

To explain the stark difference in the electronic absorption spectra, density functional theory (DFT) modeling of $[(^{t\mathrm{Bu}}\mathbf{L})_2\mathrm{Co}]^+$, $(^{t\mathrm{Bu}}\mathbf{L})_2\mathrm{Ni}$ and $[(^{t\mathrm{Bu}}\mathbf{L})_2\mathrm{Ga}]^+$ was undertaken in order to compare their electronic structures with that of $[(^{t\mathrm{Bu}}\mathbf{L})_2\mathrm{Fe}]^{n+}$ (for a full discussion of the computational methodology, see the Supporting Information). The Zn congener was omitted in favor of the isoelectronic, d^{10} Ga(III) complex for ease of comparison of the optimized structure with that experimentally determined by X-ray diffraction (Table S2). The ground-state orbital energies and HOMO isosurfaces [SOMO for $(^{t\mathrm{Bu}}\mathbf{L})_2\mathrm{Ni}$] are shown in Figure 4 (see Figures S1-S3 for expanded selection of MOs). In all the complexes, low-lying, vacant ligand-based π* orbitals are present, and in each case are comprised of significant contributions from the $(\mathrm{H})\mathrm{C}{=}\mathrm{N}_{\mathrm{phen}}$ subunit of the phenanthridinyl arm of $^{t\mathrm{Bu}}\mathbf{L}$ (Table 2; Tables S4-S6). The strong electron density acceptor character of the benzannulated diarylamido ligand[48] attributed to the presence of a phenanthridine (3,4-benzoquinoline) heterocyclic unit is thus retained across the series.

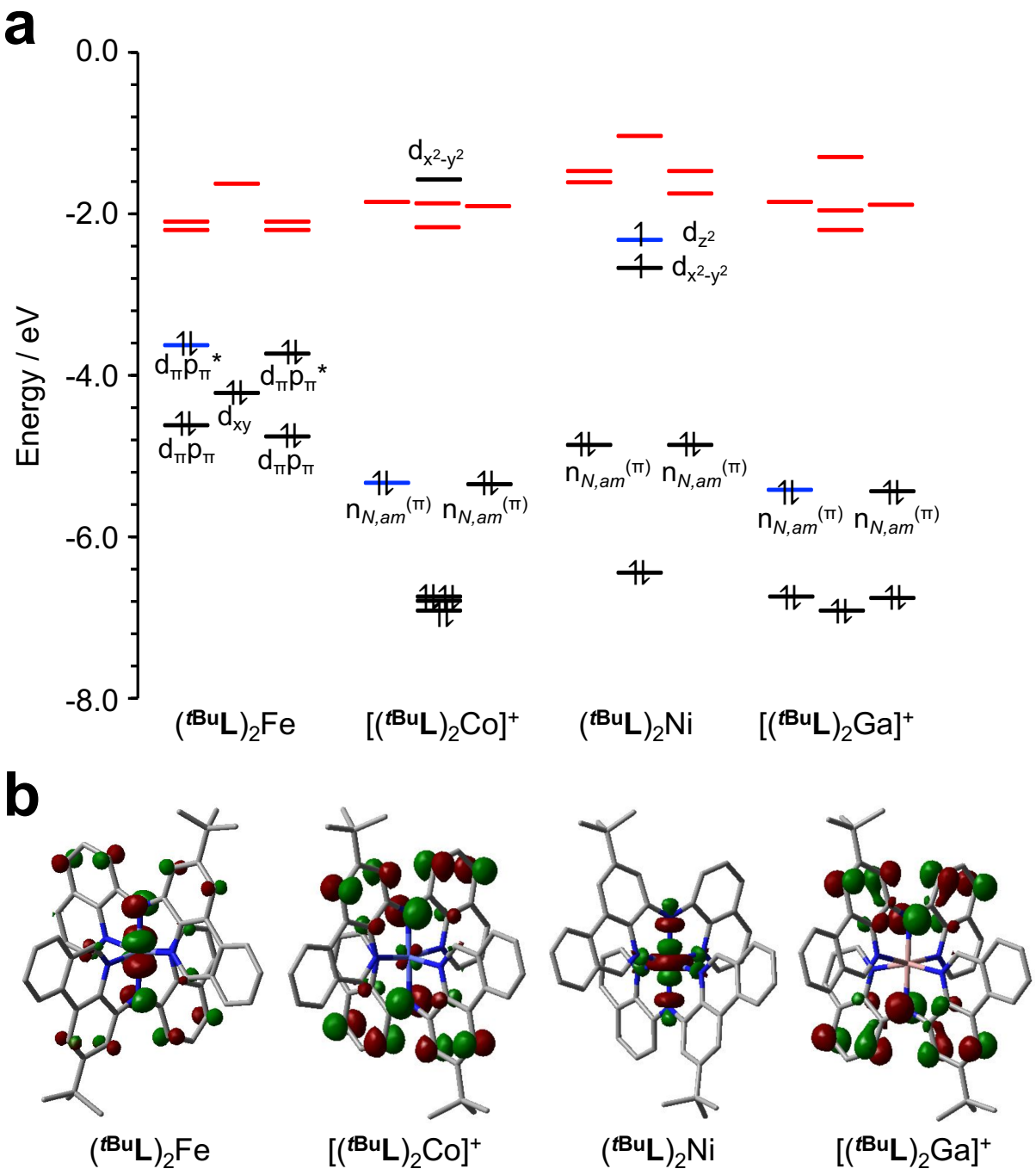

Figure 4. (a) Selections from the ground-state MO diagrams of [($^{t\mathrm{Bu}}$L)$_2$M]$^{n+}$ comparing the relative energies of the metal *d*-orbitals, N_{amido} lone pairs, and ligand-based π* orbitals (highlighted in red); (b) Isosurfaces of the highest energy occupied or partially occupied MOs highlighted in (a) in blue. For M = Fe, SMD-rM06L/6-31+G(d,p) single point at the SMD-rO3LYP/6-31+G(d,p) optimized

geometry; M = Co, Ga, SMD-rPBE0/6-31+G(d,p) single point at the SMD-rO3LYP/6-31+G(d,p) optimized geometry; M = Ni, SMD-uPBE0/6-31+G(d,p) single point at the SMD-uO3LYP/6-31+G(d,p) optimized geometry.

Table 2. Fragment contributions to the frontier molecular orbitals (MOs).[a]

	MO	M	N_{amido}	$HC{=}N_{phen}$	$HC{=}N_{quin}$	Ar_{phen}	Ar_{quin}
	LUMO+1	11	1	19	9	33	22
$(^{t\mathrm{Bu}}\mathbf{L})_2\mathrm{Fe}$ [28, b]	**LUMO**	3	1	28	6	49	14
$S = 0$	**HOMO**	48	10	4	4	15	18
	HOMO-1	56	10	4	4	12	14
	LUMO+1	1	1	33	2	56	6
$[(^{t\mathrm{Bu}}\mathbf{L})_2\mathrm{Co}]^+$ [c]	**LUMO**	3	1	19	14	31	31
$S = 0$	**HOMO**	3	19	4	3	34	36
	HOMO-1	3	20	4	3	34	36
	LUMO+1	1	1	28	4	51	14
$(^{t\mathrm{Bu}}\mathbf{L})_2\mathrm{Ni}$ [d]	**LUMO**	2	1	22	10	38	26
$S = 1$	**SOMO 1**	80	9	3	3	2	2
	SOMO 2	84	0	6	6	1	1
	LUMO+1	1	1	36	1	58	1
$[(^{t\mathrm{Bu}}\mathbf{L})_2\mathrm{Ga}]^+$ [c]	**LUMO**	1	1	21	13	34	29
$S = 0$	**HOMO**	1	19	3	3	35	37
	HOMO-1	1	19	3	3	35	37

[a] See Figures S1-S3 for relevant ground state MO isosurfaces.
[b] SMD-rM06L/6-31+G(d,p) single point at the SMD-rO3LYP/6-31+G(d,p) optimized geometry.
[c] SMD-rPBE0/6-31+G(d,p) single point at the SMD-rO3LYP/6-31+G(d,p) optimized geometry.
[d] SMD-roPBE0/6-31+G(d,p) single point at the SMD-rO3LYP/6-31+G(d,p) optimized geometry.

In the ferrous complex $(^{t\mathrm{Bu}}\mathbf{L})_2\mathrm{Fe}$, the two highest-energy occupied orbitals (HOMO, HOMO–1) represent π-anti-bonding overlap between filled orbitals at the metal center and the amido lone pairs [(d+p)π*].[28] Population analysis reports 10% N_{amido} character in both the HOMO and HOMO-1 alongside significant metal contributions (~50%; Table 2). The HOMO–2 in contrast is localized at the iron (~67%) and has predominantly non-bonding character, while the

HOMO-3 and HOMO-4 present the corresponding π-bonding overlap. Thus, $(^{tBu}\mathbf{L})_2$Fe can be described as an intermediate case of the 'HOMO inversion' model, with significant mixing between the N(2p) and Fe(3d) orbitals of appropriate symmetry. This results in the *d*-orbital manifold covering a broader spread of energy levels, causing a considerable contraction of the HOMO-LUMO gap and additional transitions in the visible responsible for the observed broad, panchromatic absorption. In the isoelectronic $3d^6$ complex $[(^{tBu}\mathbf{L})_2Co][PF_6]$, on the other hand, the lower energy *d*-orbitals of π symmetry do not mix as strongly with the N_{amido} *p*-type orbitals due to the greater disparity in energies. The HOMO and HOMO-1 of $[(^{tBu}\mathbf{L})_2Co][PF_6]$ are accordingly each comprised of only 3% metal character with stronger contributions from the two N_{amido} centers (~20%; Figure 4b), consistent with a ligand-based HOMO and HOMO-1 and a more complete case of 'HOMO inversion'. When the central metal is replaced with a $3d^{10}$ Ga(III) cation, the occupied *d*-orbitals of $[(^{tBu}\mathbf{L})_2Ga]^+$ are now all stabilized to the extent where the highest occupied orbitals, the HOMO and HOMO-1, have even more negligible contributions from the metal center (~1%) and are again largely comprised of N_{amido} lone pair character (19%) with significant contributions as well from the C_6 rings directly attached to the amido donors (~36% per ring). A similar electronic structure was reported for related pseudo-octahedral Ga(III) complexes of *bis*(pyrazolyl)amido ligands.[49]

While the fully occupied *d*-orbitals of $[(^{tBu}\mathbf{L})_2Ni]$ are also lower in energy than the N_{amido} lone pairs, single point calculations at the optimized triplet ground-state geometry using the restricted open-shell Kohn-Sham (ROKS) formalism reveal that the nearly degenerate d_z^2 (80%) and d_x^2-$_y^2$ (84%) in the d^8 Ni(II) structure contribute very strongly to the singly occupied molecular orbitals (SOMOs; Figures 4b and S4). Consistent with this, Evans' method measures a μ_{eff} = 2.90 μ_B corresponding to two unpaired electrons and a triplet ground state. A calculated spin density

map isolates the majority of this spin to the Ni metal center (Figure S5). In comparison, square-planar Ni complexes of dithiolene ligands bearing protonated pyrazine moieties show strong dπ-pπ hybridization, which only diminishes when the 3d metal is replaced by a heavier element such as Pt.[50] There, modulation of the HOMO energy level in the Ni(II) complex is sufficient to control proton-electron coupling in protonation reactions. Here, the energies of the filled π-type orbitals of diarylamido fragments do not closely enough match those of the appropriate symmetry within the Ni(II) ion's 3d manifold to engender substantial mixing.

Simulations of the absorption spectra using time-dependent DFT (TD-DFT) for each compound were found to give good agreement with experimental data (Figures S6-S13). For $[(^{t\mathrm{Bu}}\mathbf{L})_2\mathrm{Co}]^+$, $(^{t\mathrm{Bu}}\mathbf{L})_2\mathrm{Ni}$ and $[(^{t\mathrm{Bu}}\mathbf{L})_2\mathrm{Ga}]^+$, the prominent absorption bands in the visible region of the spectra can all be assigned to electronic excitations largely involving the degenerate HOMO and HOMO-1 (Tables S7-S9). As noted, these MOs contain significant contributions from the N_{amido} lone pairs ($[(^{t\mathrm{Bu}}\mathbf{L})_2\mathrm{Co}]^+$ = 19%, $(^{t\mathrm{Bu}}\mathbf{L})_2\mathrm{Ni}$ = 20%, $[(^{t\mathrm{Bu}}\mathbf{L})_2\mathrm{Ga}]^+$ = 19%). In agreement with ground-state DFT calculations, the π*-orbitals of the phenanthridine arms serve as the acceptor orbitals for transitions at lower energies (λ > 460 nm). Higher energy excitations (λ < 460 nm) populate orbitals that are largely localized on the quinoline arms of the ligand, consistent with phenanthridine offering more energetically accessible acceptor orbitals.[51] Altogether, the majority of absorptions observed in the visible region of the spectra of $[(^{t\mathrm{Bu}}\mathbf{L})_2\mathrm{Co}]^+$, $(^{t\mathrm{Bu}}\mathbf{L})_2\mathrm{Ni}$ and $[(^{t\mathrm{Bu}}\mathbf{L})_2\mathrm{Ga}]^+$ are mainly comprised of ligand-to-ligand charge-transfer character (LLCT) consistent with the experimentally observed strong ε values.

One way of explaining the similarities in both the absorption profile and redox behavior (*vide infra*) of $(^{t\mathrm{Bu}}\mathbf{L})_2\mathrm{Ni}$ compared to those of $[(^{t\mathrm{Bu}}\mathbf{L})_2\mathrm{Co}]^+$ and $[(^{t\mathrm{Bu}}\mathbf{L})_2\mathrm{Ga}]^+$ despite the presence of nearly degenerate metal-based SOMOs in $(^{t\mathrm{Bu}}\mathbf{L})_2\mathrm{Ni}$, is to consider non-Aufbau behavior upon

electromagnetic excitation or reduction/oxidation,[52] as has been described for vanadium complexes supported by porphyrinate and phthalocyanine ligands.[53] In such cases, a decrease in electron-electron repulsion promotes both removal and excitation of an electron from a doubly occupied (ligand-based) orbital versus from the metal-based SOMOs, and charge transfer into fully vacant ligand-based orbitals before the metal-based SOMOs. Another possible description is that, electronically, the complex behaves as an isolated Ni(II) ion within an pseudo-octahedral NiN_6 coordination environment that only weakly interacts with the ligand π-system, as has been invoked for related Ni(II) complexes of diarylamido ligands with flanking pyrazolyl donors.[54]

As a result, [($^{t\mathrm{Bu}}$**L**)$_2$Co][PF_6], ($^{t\mathrm{Bu}}$**L**)$_2$Ni, ($^{t\mathrm{Bu}}$**L**)$_2$Zn and [($^{t\mathrm{Bu}}$**L**)$_2$Ga][PF_6] all show similar anodic redox behavior, with two closely spaced quasi-reversible or irreversible oxidation events observed at ~ -0.05 V vs $FcH^{0/+}$ for the neutral parent species and between 0.3-0.6 V for the monocations (Figure 5, Table 1). Metal-N_{amido} (d+p)π mixing stabilizes the radicals formed by these oxidations, and the events observed for [($^{t\mathrm{Bu}}$**L**)$_2$Co][PF_6] (and ($^{t\mathrm{Bu}}$**L**)$_2$Fe[28]) are the most reversible within the series, consistent with the smallest amount of 'naked' aminyl radical character.[55] For the Co(III) species, an electrochemically reversible reduction is observed at -1.30 V. Ligand-based reduction events are also observed for all complexes close to the edge of the solvent window (CH_3CN, ~ -2.5 V), consistent with the relatively similar calculated LUMO energies (Figure 4a).

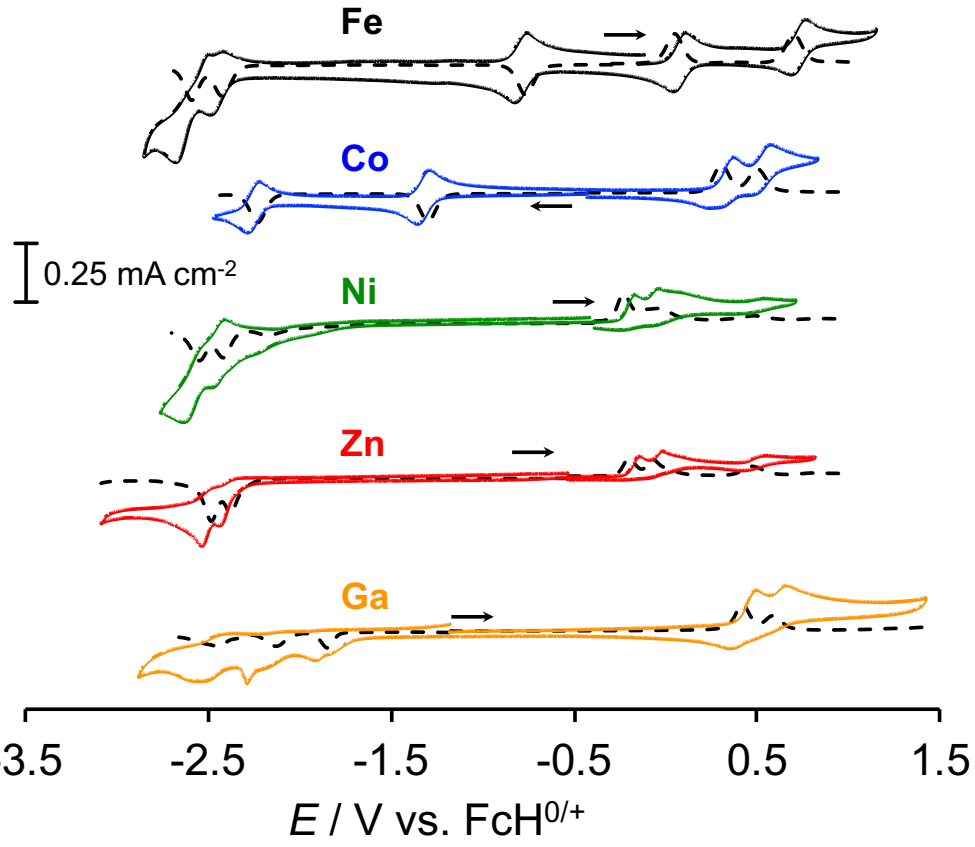

Figure 5. Cyclic voltammograms (–) and corresponding differential pulse voltammograms (---) of $[(^{t\mathbf{Bu}}\mathbf{L})_2M]^{n+}[PF_6]_n$ in CH_3CN with 0.10 M $[n\mathrm{Bu}_4N][PF_6]$ as the supporting electrolyte and a glassy carbon working electrode. CV scan rates were 100 mV s^{-1}. Potentials are listed vs. $FcH^{0/+}$.

The similar electronic structures and redox behavior of $[(^{t\mathbf{Bu}}\mathbf{L})_2M]^{n+}[PF_6]_n$ (M = Co, Ni, Zn and Ga) encouraged us to investigate oxidation of these compounds in a spectroelectrochemical cell, again for comparison with M = Fe. Each compound was dissolved in a CH_3CN solution containing $[n\mathrm{Bu}_4N][PF_6]$ electrolyte and subjected to increasingly anodic potentials while absorbance spectra were collected (Figure 6).

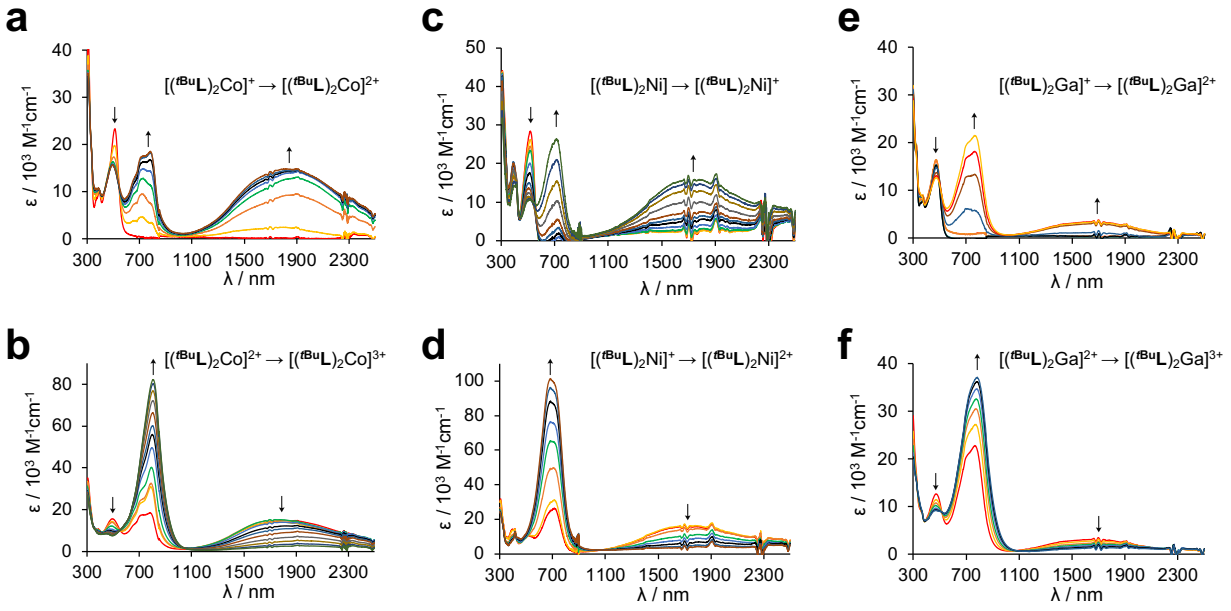

Figure 6. UV-Vis/NIR absorption spectra of $[(^{tBu}\mathbf{L})_2M]^{n+}[PF_6]_n$ in 0.3 M $[n Bu_4N][PF_6]$ CH_3CN solution: (a) M = Co, potential applied from -0.1 to 0.8 V; (b) M = Co, potential applied from 0.8 to 1.3 V; (c) M = Ni, potential applied from -0.1 to 0.35 V; (d) M = Ni, potential applied from 0.35 to 0.8 V; (e) M = Ga, potential applied from -0.1 to 1.0 V; (f) M = Ga, potential applied from 1.0 to 1.8 V.

Under these conditions, $(^{tBu}\mathbf{L})_2Zn$ suffered from rapid ligand dissociation and was not further investigated. In contrast, consistent features were seen upon oxidation of the series to $[(^{tBu}\mathbf{L})_2Co]^{2+}$, $[(^{tBu}\mathbf{L})_2Ni]^{+}$ and $[(^{tBu}\mathbf{L})_2Ga]^{2+}$. Application of mildly oxidative potentials led to the disappearance of the lowest energy band (~500 nm, Figure 6, top row), supporting the TD-DFT assignments of HOMO/HOMO-1 involvement in these transitions. In addition, a new band appeared at ~700 nm alongside an even lower energy band $[(^{tBu}\mathbf{L})_2Co]^{2+}$ = 1824 nm; $[(^{tBu}\mathbf{L})_2Ni]^{+}$ = 1769 nm; $[(^{tBu}\mathbf{L})_2Ga]^{2+}$ = 1666 nm). TD-DFT simulations of a representative spectrum, that observed for the oxidized cobalt complex $[(^{tBu}\mathbf{L})_2Co]^{2+}$ in a doublet state, are in good agreement

with experiment (S = ½; SMD-uM06L/6-31+G(d,p) single point at the SMD-uO3LYP/6-31+G(d,p) optimized geometry of $[(^{tBu}\mathbf{L})_2Co]^{2+}$; Figures S14-15, Tables S10-S11). The NIR peak (λ_{max} = 1824 nm) can be assigned largely to a HOMO(β)→LUMO(β) excitation, in which the HOMO(β) is comprised of the doubly occupied N_{amido} lone pair orbital and the LUMO(β) is the opposing phase oxidized aminyl radical (SOMO; Figure 7a). The delocalization observed in the electron-hole map (Figure 7b) is consistent with the calculated spin density map (Figure S16), which shows delocalized aminyl radical character with minimal contributions from the metal. The character of this transition can therefore be assigned as intervalence charge-transfer (IVCT) between one N_{amido} to another, across a metallic bridge. The absorption band at ~700 nm (~1.5-1.7 eV) is dominated by two states where electrons in π-orbitals of the phenanthridine and quinoline fragments respectively [HOMO-3(β), HOMO-4(β)] transfer to the SOMO.

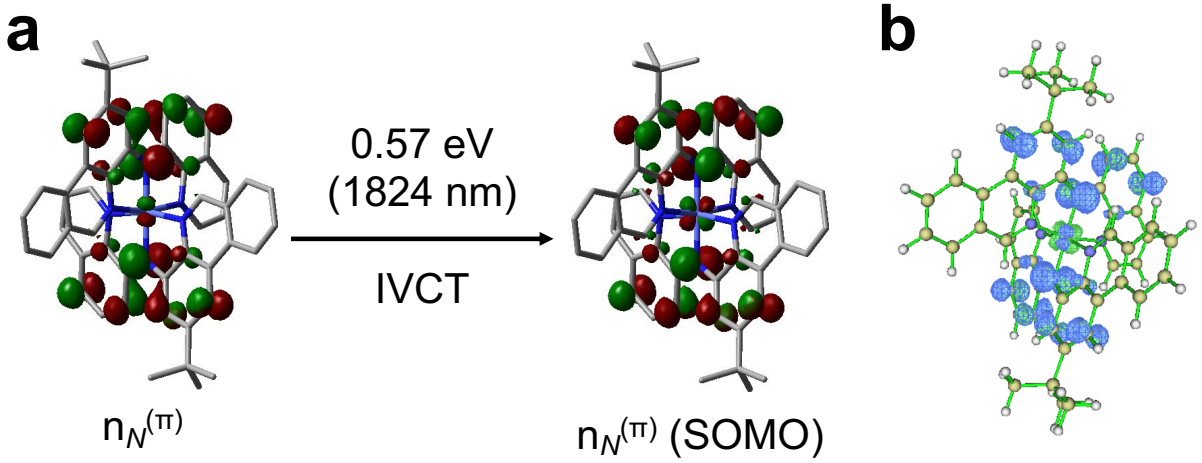

Figure 7. (a) MOs of $[(^{tBu}\mathbf{L})Co]^{2+}$ (S = ½; SMD-uM06L/6-31+G(d,p) single point at the SMD-uO3LYP/6-31+G(d,p) optimized geometry) involved in the IVCT transition. (b) TD-DFT [TD-SMD-uM06L/6-31+G(d,p) single point at the SMD-uO3LYP/6-31+G(d,p) optimized geometry] difference map calculated in acetonitrile showing electron density gain (green) and depletion (blue).

Upon further oxidation of all complexes, the peak at ~700 nm continues to grow, while the NIR peaks begin to diminish. When the spectra stopped changing with increasing applied potential, the peaks ~700 nm had significantly large ε values and the NIR absorption had completely disappeared (Figure 6, bottom row) indicative of now symmetric molecules with two aminyl radicals. This observation is consistent with the electrochemical data acquired that display two oxidations at similar potentials. While the peak positions of the oxidized complexes are similar, the intensities of the absorption bands depend significantly on the metal identity in the order $[(^{t\mathrm{Bu}}\mathbf{L})_2\mathrm{Ni}]^+ \geq [(^{t\mathrm{Bu}}\mathbf{L})_2\mathrm{Co}]^{2+} > [(^{t\mathrm{Bu}}\mathbf{L})_2\mathrm{Ga}]^{2+}$.

Together, the spectroelectrochemical and electrochemical data reveal electronic communication between the N_{amido} fragments in $[(^{t\mathrm{Bu}}\mathbf{L})_2\mathrm{Co}]^{2+}$, $[(^{t\mathrm{Bu}}\mathbf{L})_2\mathrm{Ni}]^+$ and $[(^{t\mathrm{Bu}}\mathbf{L})_2\mathrm{Ga}]^{2+}$, modulated by the metal center. Instead of one-electron oxidation events originating from isolated N_{amido} lone pairs that might be expected to occur at roughly the same potential, the second oxidation is shifted slightly anodically from the first, implying either Coulombic effects[54] or electronic communication; the appearance of an IVCT band supports the latter. Studies of homoleptic Ga complexes of di(2-3R-pyrazolyl)-*p*-arylamine ligands show similar low-energy absorption properties as a result of electronic communication between the N-amido fragments of the ligands upon oxidation of the complex.[49] Upon exchanging Ga with Ni, the communication between the amido fragments strengthens[54] owing to stronger, though still relatively weak, dπ-pπ interactions between Ni *d* orbitals and amido *p* orbitals. Using classical Marcus[56] theory along with Hush[57] relations (Tables S12-S13), the degree of communication between the electroactive N_{amido} centers can be calculated. Comproportionation constants (K_{com}) obtained from the electrochemical data suggest that $[(^{t\mathrm{Bu}}\mathbf{L})_2\mathrm{Ga}]^{2+}$ exhibits Robin-Day Class I, nearing Class II behavior,[58] while spectroelectrochemical data supports a Class IIA assignment (H_{ab} = 1284 cm^{-1}). As for the

transition metal analogs, ($^{t\mathrm{Bu}}$**L**)$_2$Ni and [($^{t\mathrm{Bu}}$**L**)$_2$Co][PF_6] show very similar behavior to each other, as well as to [($^{t\mathrm{Bu}}$**L**)$_2$Ga][PF_6]. The oxidation events are slightly better resolved resulting in a K_{com} = 1760 for both the ($^{t\mathrm{Bu}}$**L**)$_2$Ni and [($^{t\mathrm{Bu}}$**L**)$_2$Co][PF_6] complexes. They exhibit much stronger ε values (~15 000 – 20 000 M^{-1} cm^{-1}) for the low-energy IVCT band upon single oxidation, and very strong ε values (~80 000 – 100 000 M^{-1} cm^{-1}) for the vis/NIR peak (~700 nm) upon subsequent oxidation. Along with the electrochemical data, this indicates Robin-Day Class IIB (H_{ab} = 2609 cm^{-1}) and Class II-III limit behavior (H_{ab} = 2625 cm^{-1}) for [($^{t\mathrm{Bu}}$**L**)$_2$Ni]$^+$ and [($^{t\mathrm{Bu}}$**L**)$_2$Co]$^{2+}$, respectively. Compared to the homoleptic Ga and Ni complexes of pyrazolyl diarlyamido ligands mentioned above,[49,54] this series exhibits ε values nearly 20 times greater in the NIR region of the absorption spectra.

In comparison, the significant orbital overlap between the filled metal *d*-orbitals and N_{amido} lone pairs in ($^{t\mathrm{Bu}}$**L**)$_2$Fe gives rise to completely different electronic and optical properties. Unlike the rest of the series, all redox events are well separated (Figure 5). Upon oxidation of the neutral ferrous complex, the spectroelectrochemically generated spectrum of [($^{t\mathrm{Bu}}$**L**)$_2$Fe]$^+$ shows a loss in panchromatic absorption and appearance of a low-energy absorption peak (~1000 nm) in the NIR region.[28] Upon further oxidation (Figure 8), this NIR absorption decreases while a small peak at 674 nm and an intense peak (ε = 8 910 M^{-1} cm^{-1}) at 1273 nm grow in (Figure 8b). Due to the strong (d+p)π mixing, the character of the low-energy peaks for [($^{t\mathrm{Bu}}$**L**)$_2$Fe]$^+$ and [($^{t\mathrm{Bu}}$**L**)$_2$Fe]$^{2+}$ cannot be described as IVCT and Robin-Day classification is not appropriate. Instead, the low-energy peak for [($^{t\mathrm{Bu}}$**L**)$_2$Fe]$^{2+}$ can be assigned as predominantly π(d+p)-to-π*(d+p) (Fe-N_{amido}) (Tables S16-S17, Figures S17-S19) consistent with the spin density plot of the optimized dication in a triplet state (Figure S20) that shows significant radical character evenly distributed across both N_{amido} atoms as well as significant metal character. This highlights the unique electronic character

obtainable by matching the energies and symmetries of filled ligand π-orbitals and metal *d*-orbitals sufficiently closely to promote strong mixing.

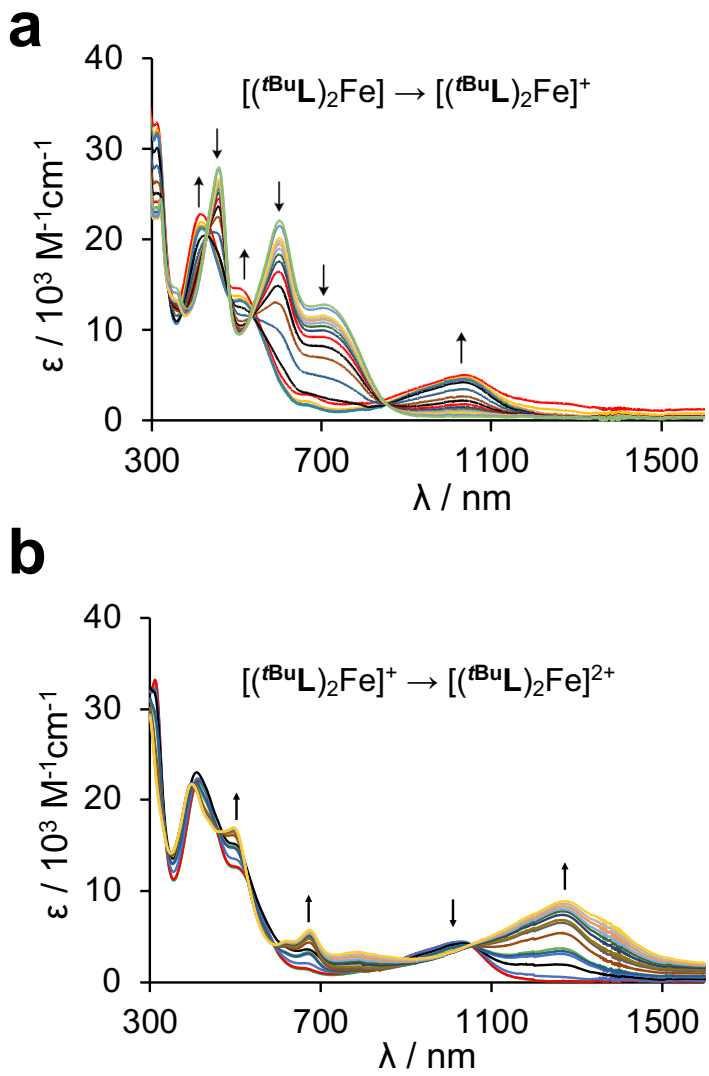

Figure 8. UV-Vis/NIR absorption spectra of $[(^{t\mathrm{Bu}}\mathbf{L})_2\mathrm{Fe}]^{n+}$ (n = 0, 1, 2) in 0.3 M $[n\mathrm{Bu_4N}][\mathrm{PF_6}]$ $\mathrm{CH_3CN}$ solution showing changes with (a) applied potential -1.8 V to -0.3 V; (b) applied potential from -0.2 to 1.0 V.

The vastly differing electronic properties of the iron congener compared to the rest of the series thus provides an experimental realization of the 'HOMO inversion'[34] design model by keeping the ligand environment constant, but varying metal *d*-orbital energies. The use of the

benzannulated ligand framework of $^{t\mathrm{Bu}}$**L** consistently provides strong absorptive cross-sections in all five MCCs, but full inversion of HOMO character from metal to ligand-centered leads to absorption profiles that attenuate at ~550 nm in their parent oxidation states, similar to what is observed in first row transition metal complexes of the 'smif' ligand with metals other than Fe or Cr.[27] When HOMO inversion from metal to more fully ligand character is achieved, strong broadband absorption in the visible and the onset of broad absorption in the NIR, however, can still be observed upon one electron oxidation (Figure 6a, c and e) which introduces aminyl radical character to the strongly absorbing benzannulated ligand framework of $^{t\mathrm{Bu}}$**L** in $[(^{t\mathrm{Bu}}\mathbf{L})_2\mathrm{Co}]^{2+}$, $[(^{t\mathrm{Bu}}\mathbf{L})_2\mathrm{Ni}]^{+}$ and $[(^{t\mathrm{Bu}}\mathbf{L})_2\mathrm{Ga}]^{2+}$. This contrasts the mixed-character HOMO observed for $(^{t\mathrm{Bu}}\mathbf{L})_2\mathrm{Fe}$, in which balanced ligand and metal-based orbital energies lead to strong mixing. This spreads out the five highest occupied MOs and broadening absorption to the edge of the visible, and oxidation to $[(^{t\mathrm{Bu}}\mathbf{L})_2\mathrm{Fe}]^{+}$ leads to diminished absorptive cross-section in general despite appearance of a new low energy absorption.[28] Engineering strong, panchromatic absorption can therefore be achieved by pairing low-lying acceptor orbitals with strongly mixed HOMOs in order to facilitate a wider energetic spread of low-energy electronic transitions, or, for an MCC with a HOMO that is more strictly ligand-based, by introduction of mixed-valent character.

CONCLUSIONS

A tridentate *N*^*N*^*N* diarylamido ligand bearing flanking benzannulated *N*-heterocyclic donors ($^{t\mathrm{Bu}}$**L**) was used to prepare deeply colored, pseudo-octahedral coordination complexes $[(^{t\mathrm{Bu}}\mathbf{L})_2\mathrm{M}]^{n+}[\mathrm{PF_6}]_n$ of a range of first-row transition and main-group metals (M = Fe, Co, Ni, Zn, Ga). Changing the identity of the ligated transition metal enables access to a gradient of electronic structures, corresponding to the 'HOMO inversion' model proposed for $[\mathrm{Fe(tpy)_2}]^{2+}$-type

complexes.[34] In particular, the different energies of the metal *d*-orbitals significantly alter the electronic structure by affecting the degree of (d+p)π mixing between filled metal orbitals and the two amido lone pairs. This engenders different photophysical properties but with consistently strong absorptions ascribable to the benzannulated ligand framework. However, instead of a steady gradient of changes corresponding to the degree of 'HOMO inversion', only the intermediate case, $(^{tBu}\mathbf{L})_2$Fe, demonstrated broad, panchromatic absorption; the remaining four MCCs showed very similar strong, but narrow, lowest energy absorption peaks. Thus, beyond the π-accepting[12] and σ-donating properties[59], the π-donating nature of a ligand framework can present an additional tool for tuning the absorption properties of MCCs which, in addition to accessing sufficiently long excited state lifetimes to facilitate charge-transport processes, is a key challenge in the development of abundant-metal photosensitizers.[60]

ACKNOWLEDGMENTS

We gratefully acknowledge the Natural Sciences Engineering Research Council of Canada for a Discovery Grant to D.E.H. (RGPIN-2014-03733); the Canadian Foundation for Innovation and Research Manitoba for an award in support of an X-ray diffractometer (CFI #32146); the University of Manitoba for the Bert & Lee Friesen Graduate Scholarship (I.B.L.) and GETS/SEGS support (J.D.B., I.B.L.); and Compute Canada for access to computational resources. Prof. Rebecca L. Davis and Prof. Viktor N. Nemykin are thanked for helpful discussions and access to spectroelectrochemical equipment (V.N.N.).

SUPPORTING INFORMATION

Tables of bond distances and angles; tabulated redox and electronic absorption parameters; computational methodology, data tables and figures; multi-nuclear NMR of all new compounds; crystallographic information files containing all X-ray data. CCDC 2022989-2022991 contain the supplementary crystallographic data for this paper. The data can be obtained free of charge from The Cambridge Crystallographic Data Center via www.ccdc.cam.ac.uk/structures.

The following files are available free of charge:

Supporting Information File (PDF)

Crystallographic Information Files (CIF)

CONFLICT OF INTERESTS DISCLOSURE

There are no conflicts of interest to declare.

AUTHOR INFORMATION

Corresponding Author

David E. Herbert (david.herbert@umanitoba.ca)

ORCIDs

Jason D. Braun: 0000-0002-5850-8048

Issiah B. Lozada: 0000-0002-1689-2918

David E. Herbert: 0000-0001-8190-2468

Author Contributions

The manuscript was written through contributions of all authors. All authors have given approval to the final version of the manuscript.

REFERENCES

(1) Hagfeldt, A.; Boschloo, G.; Sun, L.; Kloo, L.; Pettersson, H. Dye-Sensitized Solar Cells. *Chem. Rev.* **2010**, *110*, 6595–6663.

(2) O'Regan, B.; Grätzel, M. A Low-Cost, High-Efficiency Solar Cell Based on Dye-Sensitized Colloidal TiO_2 Films. *Nature* **1991**, *353*, 737–740.

(3) Strieth-Kalthoff, F.; James, M. J.; Teders, M.; Pitzer, L.; Glorius, F. Energy Transfer Catalysis Mediated by Visible Light: Principles, Applications, Directions. *Chem. Soc. Rev.* **2018**, *47*, 7190–7202.

(4) Gust, D.; Moore, T. A.; Moore, A. L. Solar Fuels via Artificial Photosynthesis. *Acc. Chem. Res.* **2009**, *42*, 1890–1898.

(5) Ponseca, C. S.; Chábera, P.; Uhlig, J.; Persson, P.; Sundström, V. Ultrafast Electron Dynamics in Solar Energy Conversion. *Chem. Rev.* **2017**, *117*, 10940–11024.

(6) Pashaei, B.; Shahroosvand, H.; Graetzel, M.; Nazeeruddin, M. K. Influence of Ancillary Ligands in Dye-Sensitized Solar Cells. *Chem. Rev.* **2016**, *116*, 9485–9564.

(7) Zhang, Y.; Lee, T. S.; Favale, J. M.; Leary, D. C.; Petersen, J. L.; Scholes, G. D.; Castellano, F. N.; Milsmann, C. Delayed Fluorescence from a Zirconium(IV) Photosensitizer with Ligand-to-Metal Charge-Transfer Excited States. *Nat. Chem.* **2020**, *12*, 345–352.

(8) Baslon, V.; Harris, J. P.; Reber, C.; Colmer, H. E.; Jackson, T. A.; Forshaw, A. P.; Smith, J. M.; Kinney, R. A.; Telser, J. Near-Infrared $^2E_g \rightarrow {}^4A_{2g}$ and Visible LMCT Luminescence from a Molecular *Bis* -(Tris(Carbene)Borate) Manganese(IV) Complex. *Can. J. Chem.* **2017**, *95*, 547–552.

(9) Dorn, M.; Kalmbach, J.; Boden, P.; Päpcke, A.; Gómez, S.; Förster, C.; Kuczelinis, F.; Carrella, L. M.; Büldt, L. A.; Bings, N. H.; Rentschler, E.; Lochbrunner, S.; González, L.; Gerhards, M.; Seitz, M.; Heinze, K. A Vanadium(III) Complex with Blue and NIR-II Spin-Flip Luminescence in Solution. *J. Am. Chem. Soc.* **2020**, *142*, 7947–7955.

(10) Robertson, N. Optimizing Dyes for Dye-Sensitized Solar Cells. *Angew. Chem., Int. Ed.* **2006**, *45*, 2338–2345.

(11) Prier, C. K.; Rankic, D. A.; MacMillan, D. W. C. Visible Light Photoredox Catalysis with Transition Metal Complexes: Applications in Organic Synthesis. *Chem. Rev.* **2013**, *113*, 5322–5363.

(12) Wang, P.; Klein, C.; Humphry-Baker, R.; Zakeeruddin, S. M.; Grätzel, M. A High Molar Extinction Coefficient Sensitizer for Stable Dye-Sensitized Solar Cells. *J. Am. Chem. Soc.* **2005**, *127*, 808–809.

(13) Kjær, K. S.; Kaul, N.; Prakash, O.; Chábera, P.; Rosemann, N. W.; Honarfar, A.; Gordivska, O.; Fredin, L. A.; Bergquist, K.-E.; Häggström, L.; Ericsson, T.; Lindh, L.; Yartsev, A.; Styring, S.; Huang, P.; Uhlig, J.; Bendix, J.; Strand, D.; Sundström, V.; Persson, P.; Lomoth, R.; Wärnmark, K. Luminescence and Reactivity of a Charge-Transfer Excited Iron Complex with Nanosecond Lifetime. *Science* **2019**, *363*, 249–253.

(14) Pal, A. K.; Li, C.; Hanan, G. S.; Zysman-Colman, E. Blue-Emissive Cobalt(III) Complexes and Their Use in the Photocatalytic Trifluoromethylation of Polycyclic Aromatic Hydrocarbons. *Angew. Chem. Int. Ed.* **2018**, *57*, 8027-8031.

(15) Whittemore, T. J.; Millet, A.; Sayre, H. J.; Xue, C.; Dolinar, B. S.; White, E. G.; Dunbar, K. R.; Turro, C. Tunable Rh_2(II,II) Light Absorbers as Excited-State Electron Donors and Acceptors Accessible with Red/Near-Infrared Irradiation. *J. Am. Chem. Soc.* **2018**, *140*, 5161–5170.

(16) Tang, Z.; Chang, X.-Y.; Wan, Q.; Wang, J.; Ma, C.; Law, K.-C.; Liu, Y.; Che, C.-M. Bis(Tridentate) Iron(II) Complexes with a Cyclometalating Unit: Photophysical Property Enhancement with Combinatorial Strong Ligand Field Effect. *Organometallics* **2020**, *39*, 2791–2802.

(17) He, M.; Ji, Z.; Huang, Z.; Wu, Y. Molecular Orbital Engineering of a Panchromatic Cyclometalated Ru(II) Dye for p-Type Dye-Sensitized Solar Cells. *J. Phys. Chem. C* **2014**, *118*, 16518–16525.

(18) Mengel, A. K. C.; Förster, C.; Breivogel, A.; Mack, K.; Ochsmann, J. R.; Laquai, F.; Ksenofontov, V.; Heinze, K. A Heteroleptic Push-Pull Substituted Iron(II) Bis(Tridentate) Complex with Low-Energy Charge-Transfer States. *Chem. Eur. J.* **2015**, *21*, 704–714.

(19) Kaim, W. Concepts for Metal Complex Chromophores Absorbing in the near Infrared. *Coord. Chem. Rev.* **2011**, *255*, 2503–2513.

(20) Jiang, T.; Bai, Y.; Zhang, P.; Han, Q.; Mitzi, D. B.; Therien, M. J. Electronic Structure and Photophysics of a Supermolecular Iron Complex Having a Long MLCT-State Lifetime and Panchromatic Absorption. *Proc. Natl. Acad. Sci.* **2020**, *117*, 20430–20437.

(21) Li, Z.; Leed, N. A.; Dickson-Karn, N. M.; Dunbar, K. R.; Turro, C. Directional Charge Transfer and Highly Reducing and Oxidizing Excited States of New Dirhodium(II,II) Complexes: Potential Applications in Solar Energy Conversion. *Chem. Sci.* **2014**, *5*, 727–737.

(22) Whittemore, T. J.; Sayre, H. J.; Xue, C.; White, T. A.; Gallucci, J. C.; Turro, C. New Rh_2 (II,II) Complexes for Solar Energy Applications: Panchromatic Absorption and Excited-State Reactivity. *J. Am. Chem. Soc.* **2017**, *139*, 14724–14732.

(23) Whittemore, T. J.; Xue, C.; Huang, J.; Gallucci, J. C.; Turro, C. Single-Chromophore Single-Molecule Photocatalyst for the Production of Dihydrogen Using Low-Energy Light. *Nat. Chem.* **2020**, *12*, 180–185.

(24) Mountford, H. S.; Spreer, L. O.; Otvos, J. W.; Calvin, M.; Brewer, K. J.; Richter, M.; Scott, B. Structure and Properties of a Bimetallic Complex with a Conjugated Bridge between Iron Atoms in Two Macrocycles. *Inorg. Chem.* **1992**, *31*, 717–718.

(25) Spreer, L. O.; Allan, C. B.; MacQueen, D. B.; Otvos, J. W.; Calvin, M. Evidence for a New Valence-Averaged Mixed-Valence Diruthenium Complex. *J. Am. Chem. Soc.* **1994**, *116*, 2187–2188.

(26) Higashino, T.; Imahori, H. Porphyrins as Excellent Dyes for Dye-Sensitized Solar Cells: Recent Developments and Insights. *Dalton Trans.* **2015**, *44*, 448–463.

(27) Frazier, B. A.; Bartholomew, E. R.; Wolczanski, P. T.; DeBeer, S.; Santiago-Berrios, M.; Abruña, H. D.; Lobkovsky, E. B.; Bart, S. C.; Mossin, S.; Meyer, K.; Cundari, T. R. Synthesis and Characterization of $(smif)_2 M^n$ (n = 0, M = V, Cr, Mn, Fe, Co, Ni, Ru; n = +1, M = Cr, Mn, Co, Rh, Ir; smif =1,3-Di-(2-pyridyl)-2-azaallyl). *Inorg. Chem.* **2011**, *50*, 12414–12436.

(28) Braun, J. D.; Lozada, I. B.; Kolodziej, C.; Burda, C.; Newman, K. M. E.; van Lierop, J.; Davis, R. L.; Herbert, D. E. Iron(II) Coordination Complexes with Panchromatic Absorption and Nanosecond Charge-Transfer Excited State Lifetimes. *Nat. Chem.* **2019**, *11*, 1144–1150.

(29) Campbell, W. M.; Burrell, A. K.; Officer, D. L.; Jolley, K. W. Porphyrins as Light Harvesters in the Dye-Sensitised TiO_2 Solar Cell. *Coord. Chem. Rev.* **2004**, *248*, 1363–1379.

(30) Boyle, N. M.; Rochford, J.; Pryce, M. T. Thienyl—Appended Porphyrins: Synthesis, Photophysical and Electrochemical Properties, and Their Applications. *Coord. Chem. Rev.* **2010**, *254*, 77–102.

(31) Campbell, W. M.; Jolley, K. W.; Wagner, P.; Wagner, K.; Walsh, P. J.; Gordon, K. C.; Schmidt-Mende, L.; Nazeeruddin, M. K.; Wang, Q.; Grätzel, M.; Officer, D. L. Highly Efficient Porphyrin Sensitizers for Dye-Sensitized Solar Cells. *J. Phys. Chem. C* **2007**, *111*, 11760–11762.

(32) Tanaka, M.; Hayashi, S.; Eu, S.; Umeyama, T.; Matano, Y.; Imahori, H. Novel Unsymmetrically π-Elongated Porphyrin for Dye-Sensitized TiO_2 Cells. *Chem. Commun.* **2007**, *20*, 2069–2071.

(33) Mathew, S.; Yella, A.; Gao, P.; Humphry-Baker, R.; Curchod, B. F. E.; Ashari-Astani, N.; Tavernelli, I.; Rothlisberger, U.; Nazeeruddin, Md. K.; Grätzel, M. Dye-Sensitized Solar Cells with 13% Efficiency Achieved through the Molecular Engineering of Porphyrin Sensitizers. *Nat. Chem.* **2014**, *6*, 242–247.

(34) Mukherjee, S.; Torres, D. E.; Jakubikova, E. HOMO Inversion as a Strategy for Improving the Light-Absorption Properties of Fe(II) Chromophores. *Chem. Sci.* **2017**, *8*, 8115–8126.

(35) Frazier, B. A.; Wolczanski, P. T.; Lobkovsky, E. B.; Cundari, T. R. Unusual Electronic Features and Reactivity of the Dipyridylazaallyl Ligand: Characterizations of $(smif)_2M$ [M = Fe, Co, Co^+, Ni; Smif = $\{(2\text{-Py})CH\}_2N$] and $[(TMS)_2NFe]_2(smif)_2$. *J. Am. Chem. Soc.* **2009**, *131*, 3428–3429.

(36) Westerhausen, M.; Kneifel, A. N. Unexpected Formation of Zinc Bis[1,3-Di(2-Pyridyl)-2-Azapropenide] during the Thermolysis of Methylzinc Bis(2-Pyridylmemyl)Amide. *Inorg. Chem. Commun.* **2004**, *7*, 763–766.

(37) Sazama, G. T.; Betley, T. A. Ligand-Centered Redox Activity: Redox Properties of 3d Transition Metal Ions Ligated by the Weak-Field Tris(Pyrrolyl)Ethane Trianion. *Inorg. Chem.* **2010**, *49*, 2512–2524.

(38) Betley, T. A.; Qian, B. A.; Peters, J. C. Group VIII Coordination Chemistry of a Pincer-Type Bis(8-Quinolinyl)Amido Ligand. *Inorg. Chem.* **2008**, *47*, 11570–11582.

(39) Glaser, F.; Wenger, O. S. Recent Progress in the Development of Transition-Metal Based Photoredox Catalysts. *Coord. Chem. Rev.* **2020**, *405*, 213129.

(40) Wenger, O. S. A Bright Future for Photosensitizers. *Nat. Chem.* **2020**, *12*, 323–324.

(41) Mandapati, P.; Braun, J. D.; Killeen, C.; Davis, R. L.; Williams, J. A. G.; Herbert, D. E. Luminescent Platinum(II) Complexes of *N^N-^N* Amido Ligands with Benzannulated *N*-Heterocyclic Donor Arms: Quinolines Offer Unexpectedly Deeper Red Phosphorescence than Phenanthridines. *Inorg. Chem.* **2019**, *58*, 14808–14817.

(42) Sheldrick, G. M. A Short History of SHELX. *Acta Crystallogr., Sect. A: Found. Crystallogr.* **2008**, *64*, 112–122.

(43) Dolomanov, O. V.; Bourhis, L. J.; Gildea, R. J.; Howard, J. A. K.; Puschmann, H. *OLEX2* : A Complete Structure Solution, Refinement and Analysis Program. *J. Appl. Crystallogr.* **2009**, *42*, 339–341.

(44) Spek, A. L. Structure Validation in Chemical Crystallography. *Acta Crystallogr., Sect. D: Biol. Crystallogr.* **2009**, *65*, 148–155.

(45) Wenger, O. S. Photoactive Complexes with Earth-Abundant Metals. *J. Am. Chem. Soc.* **2018**, *140*, 13522–13533.

(46) Wells, A. F. *Structural Inorganic Chemistry*, 5th ed.; Clarendon Press; Oxford University Press: New York, 1984.

(47) Alvarez, S. Distortion Pathways of Transition Metal Coordination Polyhedra Induced by Chelating Topology. *Chem. Rev.* **2015**, *115*, 13447–13483.

(48) Mandapati, P.; Giesbrecht, P. K.; Davis, R. L.; Herbert, D. E. Phenanthridine-Containing Pincer-like Amido Complexes of Nickel, Palladium, and Platinum. *Inorg. Chem.* **2017**, *56*, 3674–3685.

(49) Liddle, B. J.; Wanniarachchi, S.; Hewage, J. S.; Lindeman, S. V.; Bennett, B.; Gardinier, J. R. Electronic Communication Across Diamagnetic Metal Bridges: A Homoleptic Gallium(III) Complex of a Redox-Active Diarylamido-Based Ligand and Its Oxidized Derivatives. *Inorg. Chem.* **2012**, *51*, 12720–12728.

(50) Hayashi, M.; Takahashi, Y.; Yoshida, Y.; Sugimoto, K.; Kitagawa, H. Role of *d*-Elements in a Proton–Electron Coupling of *d*–π Hybridized Electron Systems. *J. Am. Chem. Soc.* **2019**, *141*, 11686–11693.

(51) Mandapati, P.; Braun, J. D.; Lozada, I. B.; Williams, J. A. G.; Herbert, D. E. Deep-Red Luminescence from Platinum(II) Complexes of *N^N–^N*-Amido Ligands with Benzannulated *N* -Heterocyclic Donor Arms. *Inorg. Chem.* **2020**, *59*, 12504–12517.

(52) Gryn'ova, G.; Coote, M. L.; Corminboeuf, C. Theory and Practice of Uncommon Molecular Electronic Configurations: Uncommon Molecular Electronic Configurations. *Wiley Interdisc. Rev.: Comput. Mol. Sci.* **2015**, *5*, 440–459.

(53) Westcott, B. L.; Gruhn, N. E.; Michelsen, L. J.; Lichtenberger, D. L. Experimental Observation of Non-Aufbau Behavior: Photoelectron Spectra of Vanadyloctaethylporphyrinate and Vanadylphthalocyanine†. *J. Am. Chem. Soc.* **2000**, *122*, 8083–8084.

(54) Hewage, J. S.; Wanniarachchi, S.; Morin, T. J.; Liddle, B. J.; Banaszynski, M.; Lindeman, S. V.; Bennett, B.; Gardinier, J. R. Homoleptic Nickel(II) Complexes of Redox-Tunable Pincer-Type Ligands. *Inorg. Chem.* **2014**, *53*, 10070–10084.

(55) Kaim, W. Manifestations of Noninnocent Ligand Behavior. *Inorg. Chem.* **2011**, *50*, 9752–9765.

(56) Marcus, R. A.; Sutin, N. Electron Transfers in Chemistry and Biology. *Biochim. Biophys. Acta* **1985**, *811*, 265–322.

(57) Hush, N.S. Intervalence-Transfer Absorption. Part 2. Theoretical Considerations and Spectroscopic Data. *Prog. Inorg. Chem.* **1967**, *8*, 391–444.

(58) Zanello, P.; Fabrizi de Biani, F.; Nervi, C. The Electrochemical Behaviour of First Row Transition Metal Metallocenes. In *Inorganic Electrochemistry*; Royal Society of Chemistry: Cambridge, 2007; pp 159–216.

(59) Liu, Y.; Warnmark, K.; Liu, Y.; Sundstrom, V.; Persson, P. Fe *N*-Heterocyclic Carbene Complexes as Promising Photosensitizers. *Acc. Chem. Res.* **2016**, *49*, 1477–1485.

(60) Shon, J.-H.; Teets, T. S. Molecular Photosensitizers in Energy Research and Catalysis: Design Principles and Recent Developments. *ACS Energy Lett.* **2019**, *4*, 558–566.

FOR TABLE OF CONTENTS ONLY

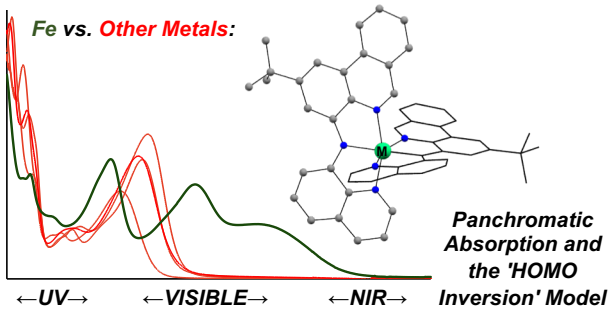

TOC SYNOPSIS

A series of deeply colored metal coordination complexes supported by a tridentate *N*^*N*-^*N* diarylamido ligand bearing flanking benzannulated *N*-heterocyclic donors is decribed and used to determine how the 'HOMO inversion' model might facilitate strong, panchromatic absorption. While the Fe(II) congener exhibits broad absorption, isostructural and isoelectronic complexes of other metals show vastly different electronic properties, traced to differences in the relative energies of the ligated element's *d* orbitals and filled amido ligand π-type orbitals.